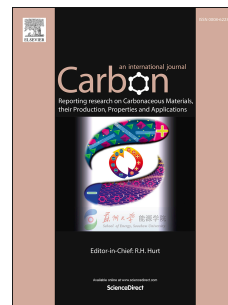


# Accepted Manuscript

Porous ZnO/Carbon nanocomposites derived from metal organic frameworks for highly efficient photocatalytic applications - A correlational study

Mian Zahid Hussain, Govinder Singh Pawar, Zheng Huang, Asif. Ali Tahir, Roland A. Fischer, Yanqiu Zhu, Yongde Xia



PII: S0008-6223(19)30126-5

DOI: <https://doi.org/10.1016/j.carbon.2019.02.013>

Reference: CARBON 13927

To appear in: *Carbon*

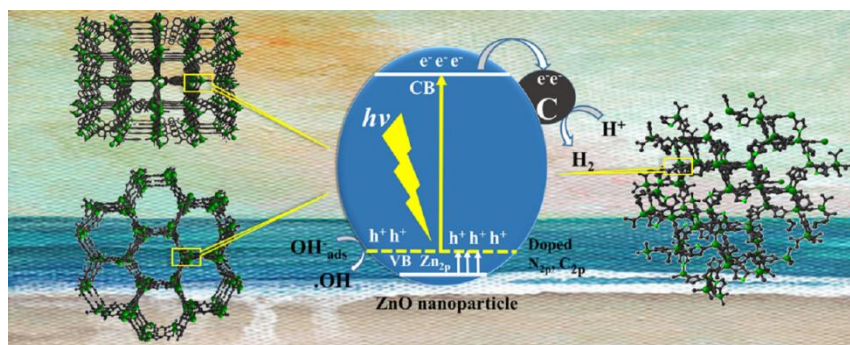
Received Date: 6 November 2018

Revised Date: 2 February 2019

Accepted Date: 4 February 2019

Please cite this article as: M.Z. Hussain, G.S. Pawar, Z. Huang, A.A. Tahir, R.A. Fischer, Y. Zhu, Y. Xia, Porous ZnO/Carbon nanocomposites derived from metal organic frameworks for highly efficient photocatalytic applications - A correlational study, *Carbon* (2019), doi: <https://doi.org/10.1016/j.carbon.2019.02.013>.

This is a PDF file of an unedited manuscript that has been accepted for publication. As a service to our customers we are providing this early version of the manuscript. The manuscript will undergo copyediting, typesetting, and review of the resulting proof before it is published in its final form. Please note that during the production process errors may be discovered which could affect the content, and all legal disclaimers that apply to the journal pertain.



**Porous ZnO/Carbon nanocomposites derived from metal organic frameworks  
for highly efficient photocatalytic applications - A correlational study**

Mian Zahid Hussain,<sup>a, b</sup> Govinder Singh Pawar<sup>c</sup>, Zheng Huang<sup>a</sup>, Asif. Ali Tahir<sup>c</sup>, Roland A. Fischer,<sup>b</sup> Yanqiu Zhu,<sup>a</sup> and Yongde Xia<sup>\*, a</sup>

<sup>a</sup> College of Engineering, Mathematics and Physical Sciences, University of Exeter, Exeter EX4 4QF, United Kingdom

<sup>b</sup> Catalysis Research Center, Department of Chemistry, Technical University of Munich, Ernst-Otto-Fischer- Straße 1, 85748 Garching, Germany

<sup>c</sup> Environment and Sustainability Institute, University of Exeter, Penryn Campus, Penryn, TR10 9FE, United Kingdom

\* Corresponding author. Tel: +44 1392 723683.

*Email address:* Y.Xia@exeter.ac.uk (Yongde Xia)

**ABSTRACT**

Porous ZnO/C nanocomposites derived from 3 different Zinc based metal-organic frameworks (MOFs) including MOF-5, MOF-74 and ZIF-8, were prepared at high temperature under water-steam atmosphere and their performances in photocatalytic H<sub>2</sub> evolution reaction (HER) and photodegradation of organic dye pollutants were evaluated. The formation mechanism from MOF precursors, the structural properties, morphologies, compositions and textural properties of the derived ZnO/C composites were fully investigated based on different characterization techniques and the correlation between the precursors and the derived composites was discussed. It is evident that MOF precursors determine the crystalline structures, doping profiles, thermal stabilities and metal oxide-carbon weight percentage ratios of the resulting composites. The correlation between MOFs and their derived nanocomposites indicates that different parameters play unlike roles in photocatalytic performances. The desired properties can be tuned by selecting appropriate MOF precursors. MOF-5 derived porous ZnO/C nanocomposite not only exhibits the highest photocatalytic dye degradation activity under visible light among these MOFs, but also outperforms those derived from MOF-74 and ZIF-8 up to 9 and 4 times in photocatalytic HER respectively. This study offers simple and environmentally friendly approaches to further develop new homogeneously dispersed functional metal oxide/carbon composites for various energy and environment-related applications.

## 1. Introduction

In the past 15 years, Metal-Organic Frameworks (MOFs) have emerged as one of the most exciting advanced materials due to their exceptional textural properties, high thermal stabilities and a wide range of promising applications in gas storage and separation, carbon capture, supercapacitors, sensing, catalysis and energy applications.[1-7] MOFs are constructed by linking metal-containing secondary building units (SBU) with organic linkers through strong coordination bonds (reticular synthesis) to form highly porous crystalline framework.[8] In particular, Zn and Ti based MOFs are considered to be excellent materials for energy and environmental applications such as fuel cells, photocatalytic degradation of toxic organic dyes in industrial wastewater and as catalytic materials for H<sub>2</sub> evolution reactions (HER) and O<sub>2</sub> evolution reactions (OER) in water splitting.[9-13] However, many MOFs are not stable upon interacting with water molecules. Moreover, they exhibit wide energy band gaps which limit their potential to replace conventional metal oxide nanoparticles based photocatalysts.

On the other hand, the conventional metal oxide photocatalysts also face serious limitations due to their low surface areas, agglomerations of particles and inadequate active sites. To overcome these challenges, researchers make efforts to synthesize metal-oxide/carbon composites, which may be highly efficient in photocatalytic applications due to the potential to tune the energy band gap of the composites.[14, 15] However, the physical and mechanical mixing approaches do not produce a homogeneous distribution of metal oxides in a carbon matrix. Therefore, poor interfacial contacts between metal-oxide and carbon result in meagre photocatalytic performances of those composites. In the past several years, metal-oxide/carbon composites derived from MOFs emerged as a new technique to obtain homogeneously distributed metal oxide nanoparticles in a highly porous carbon matrix. The carbonization of MOFs at high temperatures (above the Tamman temperature and below the boiling point of the actual metal species from which a MOF is constructed) under inert gaseous atmospheres (i.e. Ar, N<sub>2</sub>) can generate metal oxide/carbon composites with desired topologies, controllable morphologies and functionalities as well as tuneable energy band gaps.[16-19] In 2012, Das *et al.* found that if the MOFs consist of Co, Cu or Ni metal ions with reduction potential of - 0.27 V or higher, pure metal nanoparticles are formed upon calcination up to 900 °C in an inert (e.g. N<sub>2</sub>) environment, whereas Zn, Mn, Mg, Cr or Al metal ions with reduction potential lower than -

0.27 V can combine with oxygen presented in the MOFs and form metal oxide nanoparticles in the calcination process.[20] Meanwhile, amorphous carbons formed from the carbonization of organic linker during the pyrolysis process, which encapsulate the metal or metal oxide nanoparticles and preserve the morphology of parental MOFs with high surface areas and pore structures.

Water steam is regarded as a weak oxidizing agent that can result in slow oxidation rate, therefore the mild and fine controllable oxidation process in water vapor atmosphere during the carbonization of MOFs at high temperatures will not compromise the structures and properties of the target materials.[21, 22] This is especially true when water vapor is used as an oxidation agent during the generation of porous carbon-metal oxide composites since water vapor can react with and oxidize the formed carbons at high temperatures to introduce hydrophilic functional groups like -COOH on the surface of carbons, which may improve their photocatalytic performance.[21, 22]

A number of studies have been reported on the MOFs derived ZnO/C nanocomposites for photocatalytic and photoelectrochemical H<sub>2</sub> evolution. For example, Zn-based MOFs such as MOF-5, MOF-74 and ZIF-8 can generate robust high surface area ZnO/C composites with cubic, spherical and hexagonal morphologies respectively. Those MOFs derived composites were characterized by typical techniques and photocatalytic applications of these derivatives were reported.[21, 23-27] However, there is no study available that explores the correlation between MOF precursors and their derived ZnO/C composites.

It is of utmost importance to understand that how the transformation from MOFs to ZnO/C takes place upon high-temperature calcination in a certain gaseous atmosphere. During the carbonization process, how does the MOF decomposition lead to the formation of metal oxide/carbon structures and what is the relationship between those different ZnO/C composites with their photocatalytic performance? In this present study, we will try to address these questions via systemic investigation of the formation of ZnO/C composites upon carbonization of three different zinc based MOF precursors such as MOF-5, MOF-74 and ZIF-8. Built on the understanding of the role of crystal structures and morphologies of the MOF precursors, in this comparison study, we will correlate some primary parameters such as crystallinity of derived composites, metal oxide and carbon compositions, structural and textural properties, nitrogen (N)

and carbon (C) doping, functionalities attached on the surface of the composites and their chemical properties, and understand their contribution and role in photocatalytic performance of these MOFs derived ZnO/C composites. Moreover, the research findings from this work combined with a better understanding of the structure-application relationship of the studied materials will help to build up and select appropriate precursors that can derive controllable metal oxide/carbon composites with required properties for specific applications.

## 2. Experimental

All the chemicals for the synthesis of MOF-5, MOF-74 and ZIF-8 were purchased from Sigma-Aldrich and directly used without further purification.

### 2.1 Synthesis of MOF precursors

MOF-5 was synthesized at room temperature following a slightly modified literature reported method.[28] Typically, 48 mM of  $\text{Zn}(\text{NO}_3)_2 \cdot 6\text{H}_2\text{O}$  and 24 mM of terephthalic acid ( $\text{H}_2\text{BDC}$ ) combined with 19 mL of triethylamine (TEA) was dissolved in 450 mL of dimethylformamide (DMF) in a 500 mL screw jar. The mixed solution was constantly stirred at room temperature for 20 hours. Then the white product was collected by centrifugation after washed twice with DMF to remove the undissolved species. The collected white powder was further washed with chloroform twice and then immersed in chloroform overnight. The obtained product was dried in a vacuum oven at 80 °C overnight.

MOF-74 was prepared as follows: with 3:1 molar ratio, 39 mM of  $\text{Zn}(\text{NO}_3)_2 \cdot 6\text{H}_2\text{O}$  and 13 mM of 2,5-dihydroxyterephthalic acid ( $\text{H}_4\text{DOBDC}$ ) were dissolved in 500 mL of DMF and 25 mL of distilled water. The mixed solution was placed in an oil bath at 110 °C for 20 hours upon constant stirring. The greenish color product was first washed with DMF twice to remove the unreacted species, followed by washed with methanol twice, and then immersed in methanol overnight.[28] The final product was collected by centrifugation and dried in a vacuum oven at 70 °C overnight.

ZIF-8 was synthesized following a well-established procedure.[29] Typically, 16 mM of  $\text{Zn}(\text{NO}_3)_2 \cdot 6\text{H}_2\text{O}$  and 800 mM of 2-methylimidazole were dissolved in 400 mL of distilled water.

The mixed solution was stirred at room temperature for 20 hours. The white ZIF-8 nanocrystals were collected and washed with water three times. For solvent exchange, the white powder was first washed with methanol twice and then immersed in methanol overnight. The final product was collected by centrifugation and dried in a vacuum oven at 70 °C overnight.

## 2.2 Preparation of MOF derived ZnO/C nanocomposites

ZnO/C nanocomposites were prepared by one-step direct carbonization of precursors MOF-5, MOF-74 and ZIF-8 under water-steam atmosphere. Typically, 1 g of the dried precursor was loaded in an alumina boat and placed it at the center of a flow-through quartz tube sitting in a tube furnace. The furnace was set at a heating rate of 10 °C/min to the target temperature 800 °C. The flow rate of argon gas was set at 30 ml/min. When the furnace temperature arrived at 800 °C, water vapors were introduced via argon gas flow through a buffer bottle with water at ambient temperature and maintained the furnace temperature at 800 °C for 1 hour. Then the gas flow was switched to argon only and the furnace cooled down to room temperature. The final black products were collected from quartz tube and were named as **ZnO/C<sub>MOF-5</sub>**, **ZnO/C<sub>MOF-74</sub>** and **ZnO/C<sub>ZIF-8</sub>** respectively. For comparison, a pure ZnO sample as a reference was also derived by calcination of MOF-5 precursor in air at 800 °C for 1 hour. This sample was labeled as **ZnO<sub>Air</sub>**.

To investigate the photocatalytic contributions of ZnO nanoparticles and the porous carbon matrix towards adsorption and photodegradation of MB, re-calcination of MOF-derived composites **ZnO/C<sub>MOF-5</sub>**, **ZnO/C<sub>MOF-74</sub>** and **ZnO/C<sub>ZIF-8</sub>** was carried out in the air atmosphere. Typically, 100 mg of each MOF-derived ZnO/C sample was loaded into an alumina boat and placed at the center of flow-through quartz tube sitting in a tube furnace. The furnace was set at 5 °C/min to the target temperature of 550 °C. The MOF derived ZnO/C samples were heated for 3 hours in air. Upon cooling to the room temperature, the samples were collected to measure the photocatalytic dye degradation activity under visible light. The obtained samples were named as **ZnO<sub>MOF-5</sub>**, **ZnO<sub>MOF-74</sub>** and **ZnO<sub>ZIF-8</sub>** respectively.

## 2.3 Material Characterizations

Powder X-ray diffraction (PXRD) patterns of precursor MOFs and their derived composites were recorded by employing Bruker D8 instrument with Cu K $\alpha$  radiation (1.54 Å) (40 kV, 40 mA). The powder samples were prepared onto a glass slide by gently pressing the powder to smoothen the surface. The morphologies of the MOFs and derived composites were characterized by scanning electron microscopy (SEM) (Hitachi S3200N). High-resolution images and elemental mapping of the as-prepared composites were carried out by using transmission electron microscopy (TEM) (JEM 2100 LeB6 200 KV) equipped with energy dispersive X-ray spectroscopy (EDX). For SEM, powder samples were spread on a carbon tape and sputtered with a gold layer of 3 nm to avoid charging of samples. For TEM images and elemental mapping, the samples were dispersed in absolute ethanol under moderate sonication, then pipetted a few drops onto a holey carbon Cu grid followed by the drying in air at 70 °C overnight. Thermal stability of the composites and the weight percentage (wt. %) of metal oxide-carbon were measured by employing thermogravimetric analysis (TGA) TA SDT Q600 instrument. For typical TGA measurement, 5 mg of each sample was put into an alumina crucible and heated up to 810 °C with a heating rate of 10 °C/min under a constant air flow of 100 mL/min. To examine the nature of carbon and metal oxide species, the Raman spectra were recorded (WITec ALPHA300 R) in a range from 20 to 2000 cm<sup>-1</sup> by using 532 nm laser excitation under 6 mW. Fourier-transform infrared (FTIR) spectra of the samples were recorded with an Alpha Bruker system. To detect the peaks at lower wavenumbers, a very small amount of sample was mixed with pre-dried KBr powder with ratio 0.1:100 respectively and pressed in the form of a pallet for the FTIR analysis. The X-ray photoelectron spectroscopy (XPS) was performed using a Kratos AXIS ULTRA spectrometer with a monochromated Al KR X-ray source (1486.6 eV) operated at 10 mA emission current and 15 kV anode potential. The analysis chamber pressure was better than the 1.3x10<sup>-12</sup> bar. The take-off angle for the photoelectron analyzer was 90° and the acceptance angle was 30°. To calculate the absorption bands and energy band gaps of ZnO/C nanocomposites, UV-Vis absorption spectra were acquired by employing a Shimadzu UV-3600 Plus UV-VIS-NIR spectrophotometer. The specific surface areas (SSA) and the pore size distributions (PSD) of the composites were measured by N<sub>2</sub> sorption at -196 °C on a Quantachrome Autosorb-iQ gas sorptometer via the conventional volumetric technique. Before the surface area analysis, the samples were degassed at 200 °C for

3 hours under vacuum. The pore size distribution was determined using non-local density functional theory (NLDFT) method for slit/cylinder pores.

#### *2.4 Evaluation of photodegradation and photocatalytic activity*

The photodegradation of organic dye methylene blue (MB) by MOF derived ZnO/C composites was measured under visible light irradiation. The visible light source was provided by 8 lamps (each 20 W) with a light intensity of 120 mW/cm<sup>2</sup> (PerfectLight, 320 nm ≤ λ ≤ 780 nm). Typically, 10 mg of black ZnO/C composite was added into 50 mL (20 ppm) aqueous MB solution. After different time intervals, 1 mL aliquots were taken and the concentration of MB was determined by the UV-vis absorption spectroscopy. The subsequent photodegradation (D) of MB in aqueous solution (%) was calculated in terms of the decrease in final (C) and initial (C<sub>0</sub>) concentrations.

Hydrogen evolution reaction (HER) of as-synthesized ZnO/C composites was measured. Prior to the measurement, the powder samples were ultrasonicated for 30 minutes to break down any large particles. For each measurement, 25 mg of sample was added into 111 mL of 35 % aqueous methanol (H<sub>2</sub>O/MeOH) solution. The solution was kept in a 116 mL vessel (sealed with rubber stopper) with 5 mL dead space to collect the evolved H<sub>2</sub> gas. The solution was purged with argon gas for 30 minutes using needles upon stirring. Then the vessel was placed in front of the solar simulator under constant stirring for 6 hours. A sample of evolved gas was taken every hour using a syringe needle and manually injected into the GC to evaluate the amount of H<sub>2</sub> produced. The amount of evolved H<sub>2</sub> gas was recorded in μVS<sup>-1</sup> by GC and then converted into μmol/g.

### **3. Results and discussion**

#### *3.1 Characterizations of ZnO/C composites*

The powder X-ray diffraction (PXRD) patterns of as-synthesized MOF-5, MOF-74 and ZIF-8 are shown in Fig. 1a. The main peaks appeared at 2θ of 6.7°, 9.6° and 13.6° for MOF-5, at 6.7° and 11.7° for MOF-74 and at 7.9°, 11.9° and 14.9° for ZIF-8, confirm the formation of well crystalline structures.[23-25] MOF-5 and MOF-74 derived composites show main peaks of

crystalline ZnO at  $2\theta$  of  $31.7^\circ$ ,  $34.4^\circ$  and  $36.2^\circ$  in their PXRD patterns, which corresponds to (100), (200) and (101) of wurtzite ZnO. However, as shown in Fig. 1b, no peaks of ZnO are observed in ZIF-8 derived  $\text{ZnO}/\text{C}_{\text{ZIF-8}}$ . The absence of ZnO peaks might be due to the poor crystallinity of fine ZnO nanoparticles which are largely embedded in formed porous carbon matrix. However, a broad peak observed at around  $2\theta$  of  $24^\circ$  and a very low intensity bump at  $2\theta$  of  $44^\circ$  which can be indexed to (002) and (101) of carbon, indicate the formation of amorphous carbon upon decomposition of the organic linker. These low intensity broad peaks of carbons are suppressed in samples  $\text{ZnO}/\text{C}_{\text{MOF-5}}$  and  $\text{ZnO}/\text{C}_{\text{MOF-74}}$  due to the relatively high intensity peaks of ZnO nanoparticles. The presence of carbon in all the derived composites is confirmed by TGA, XPS and Raman (as shown below). The amplified region (Inset in Fig. 1b) shows that the relative intensity and the location of the main XRD peak at  $2\theta$  of  $36.24^\circ$  in samples  $\text{ZnO}/\text{C}_{\text{MOF-5}}$  and  $\text{ZnO}/\text{C}_{\text{MOF-74}}$  are almost identical, indicating the formation of similar crystalline structures of ZnO nanoparticles upon carbonization of MOF-5 and MOF-74 at  $800^\circ\text{C}$  in water vapor saturated argon. The PXRD patterns of ZnO derived from MOF-5 in the air ( $\text{ZnO}_{\text{Air}}$ ) exhibited highly crystalline wurtzite ZnO structures with main peak (101) appearing at  $2\theta$  of  $36.24^\circ$ , as presented in Fig. S1a of the Supplementary Data.

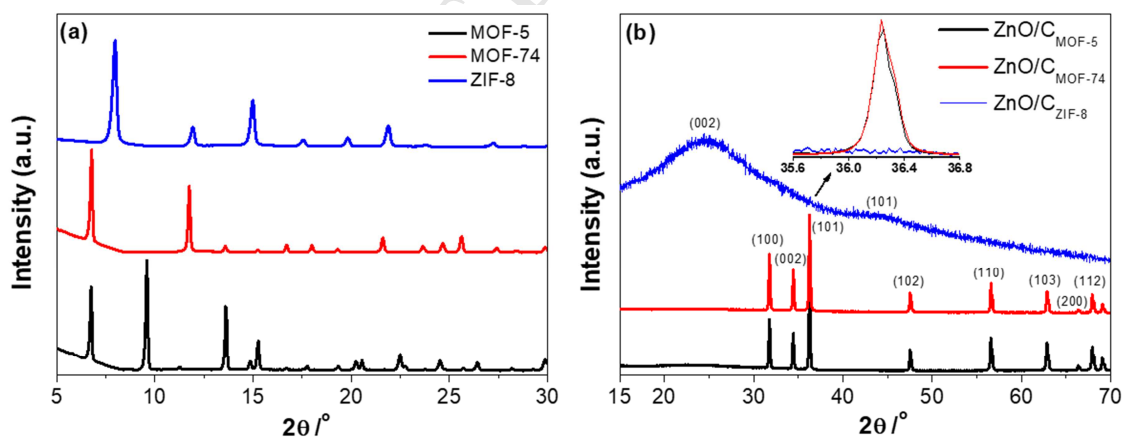


**Fig. 1** PXRD patterns of (a) as-synthesized MOFs and (b) nanocomposites  $\text{ZnO}/\text{C}$  obtained at  $800^\circ\text{C}$  under water vapors saturated argon atmosphere. **MOF-5** and  $\text{ZnO}/\text{C}_{\text{MOF-5}}$  are represented in black, **MOF-74** and  $\text{ZnO}/\text{C}_{\text{MOF-74}}$  in red while **ZIF-8** and  $\text{ZnO}/\text{C}_{\text{ZIF-8}}$  in blue respectively. Miller indices of the lattice plane reflections of the wurtzite ZnO are presented in brackets. The inset in Fig. 1b is the amplified PXRD pattern of ZnO peak (101).

The PXRD patterns of samples  $\text{ZnO}_{\text{MOF-5}}$ ,  $\text{ZnO}_{\text{MOF-74}}$  and  $\text{ZnO}_{\text{ZIF-8}}$ , which were obtained after re-calcination of samples  $\text{ZnO}/\text{C}_{\text{MOF-5}}$ ,  $\text{ZnO}/\text{C}_{\text{MOF-74}}$  and  $\text{ZnO}/\text{C}_{\text{ZIF-8}}$  in air at 550 °C for 3 hours, were recorded. As shown in Fig S1b of Supplementary Data, the main PXRD peak is shifted from  $2\theta$  of 36.24° ( $\text{ZnO}_{\text{Air}}$ ) to 36.17°, 36.19° and 36.06° for  $\text{ZnO}_{\text{MOF-5}}$ ,  $\text{ZnO}_{\text{MOF-74}}$  and  $\text{ZnO}_{\text{ZIF-8}}$  respectively. The highlighted peaks of  $\text{ZnO}_{\text{MOF-5}}$  and  $\text{ZnO}_{\text{MOF-74}}$  (Inset in Fig. S1b of Supplementary Data) also show a shoulder peak at around  $2\theta$  of 36.24°. The shift of peaks toward lower  $2\theta$  suggests a larger d-spacing (confirmed by HRTEM), which indicates the deformations in the crystal structure due to the doping of C atoms into the ZnO crystal lattice. It is interesting to observe that  $\text{ZnO}_{\text{ZIF-8}}$  obtained from the re-calcination of  $\text{ZnO}/\text{C}_{\text{ZIF-8}}$  at 550 °C under air atmosphere shows relatively lower intensity with much broader peaks, suggesting that ZIF-8 derived  $\text{ZnO}_{\text{ZIF-8}}$  nanoparticles are poorly crystalline. This poor crystallinity of ZnO nanoparticles in ZIF-8 derived composites might be due to the fact that ZnO nanoparticles are encapsulated in nitrogen-rich amorphous carbons, which is formed during pyrolysis at high temperature since no accessible oxygen species are available for Zn atoms to crystallize as ZnO nanoparticles. Moreover, the broader PXRD peaks of  $\text{ZnO}_{\text{ZIF-8}}$  with low intensity may be likely due to the co-doping of C and N heteroatoms into ZnO crystal lattice that results in the local strain in ZnO nanoparticles, which leads to the increase of the spacing between lattice fringes of ZnO (shown in Fig. S1). In addition, as shown in Fig. S2 of Supplementary Data, samples  $\text{ZnO}/\text{C}_{\text{MOF-5}}$ ,  $\text{ZnO}/\text{C}_{\text{MOF-74}}$  and  $\text{ZnO}/\text{C}_{\text{ZIF-8}}$  show clearly black color due to the presence of a large amount of carbon species. However, re-calcination of the MOF-derived ZnO/C results in  $\text{ZnO}_{\text{MOF-5}}$ ,  $\text{ZnO}_{\text{MOF-74}}$  and  $\text{ZnO}_{\text{ZIF-8}}$  which show lighter color like grey, light grey and white respectively. The variation in colors of these ZnO nanoparticles obtained from re-calcination of MOF-derived ZnO/C composites suggest the doping of more C in  $\text{ZnO}_{\text{MOF-5}}$  and  $\text{ZnO}_{\text{MOF-74}}$  whereas much less doping level of C but more N in  $\text{ZnO}_{\text{ZIF-8}}$ .

TGA was carried out under air flow (Fig. 2) to determine the thermal stabilities as well as the amount (wt. %) of metal oxide and carbon present in the precursor MOFs and their derived composites. Since the as-synthesized MOF-5, MOF-74 and ZIF-8 were obtained by washing with a solvent (such as DMF), followed by solvent exchange to remove the washing solvent, the first weight loss between 100 and 200 °C for MOFs in Fig. 2a is due to the removal of the residual solvent. As shown in the inset to Fig 2a, after drying at 70 °C overnight, there was 2.5 % chloroform and 4.5 % DMF left in the pores of MOF-5. In MOF-74, almost all the DMF was

exchanged with methanol, which evaporated (7 wt. %) below 100 °C. However, ZIF-8 showed only 2 wt. % weight loss around 150 °C due to the removal of the residual DMF in the pores.

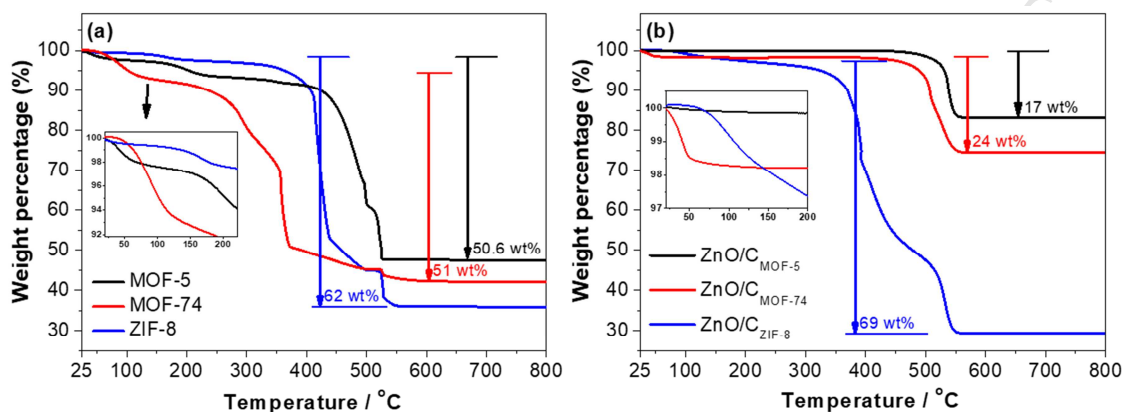


**Fig. 2** TGA profiles of (a) MOFs and (b) derived composites obtained at 800 °C under water vapors saturated argon atmosphere. **MOF-5** and **ZnO/C<sub>MOF-5</sub>** are represented in black, **MOF-74** and **ZnO/C<sub>MOF-74</sub>** in red while **ZIF-8** and **ZnO/C<sub>ZIF-8</sub>** in blue respectively.

The second major weight loss in MOFs precursor is witnessed due to the decomposition of the organic linker molecules and the evaporation of carbon (and nitrogen in ZIF-8) species in the form of CO<sub>x</sub> and NO<sub>x</sub>. The weight loss is 50.6 % for MOF-5 at 400 °C, 51 % for MOF-74 at 250 °C whereas 62 % for ZIF-8 at 350 °C respectively. The TGA profile indicates that among these MOFs, MOF-5 is thermally more stable with 47.4 wt. % of ZnO content, whereas MOF-74 is thermally least stable with residual 42 wt. % of ZnO content and ZIF-8 showed relatively moderate thermal stability with 35.8 wt. % ZnO content.[21, 25, 30]

The ZnO/C composites derived from different MOFs demonstrated interesting TGA profiles under air flow. As shown in Fig. 2b, all these composites **ZnO/C<sub>MOF-5</sub>**, **ZnO/C<sub>MOF-74</sub>** and **ZnO/C<sub>ZIF-8</sub>** show less than 2 % weight loss at a temperature below 200 °C due to the removal of adsorbed moisture. Moreover, **ZnO/C<sub>MOF-5</sub>** showed a steep weight loss of 17 wt. % at 540 °C leaving 83 wt. % of ZnO nanoparticles, while the composite **ZnO/C<sub>MOF-74</sub>** exhibited a weight loss of 24 wt. % at 520 °C. The remaining species were ZnO nanoparticles (74.5 wt. %) as confirmed by XRD. However, the **ZnO/C<sub>ZIF-8</sub>** demonstrated the highest weight loss of 69 wt.

% in two steps at 380 °C and 540 °C, maybe due to the removal of nitrogen and carbon species respectively. The residual species were ZnO nanoparticles (29 wt. %) as confirmed by XRD and XPS. In addition, no weight loss was observed in TGA measurement of  $\text{ZnO}_{\text{Air}}$ , indicating that pure ZnO is obtained under the air atmosphere (shown in Fig. S3 in Supplementary Data).

As XRD and TGA confirm that different content of ZnO and carbon are obtained upon carbonization of MOFs, the correlation between MOFs precursor and the derived ZnO/C composites can be understood through the molecular structures of secondary building units (SBUs) that are the molecular cluster of zinc ions and organic linkers which constitute a MOF. As shown in Fig. 3a, MOF-5 is constituted of SBUs where the  $\text{ZnO}_4$  tetrahedra make a tetramer cluster of  $\text{Zn}_4\text{O}(\text{CO}_2)_6$  linked through six bidentate linear benzene-1,4-dicarboxylate ( $\text{C}_8\text{H}_4\text{O}_4$ ) linkers from the ligand arranging in a cubic geometrical order.[8, 28] Upon carbonization of MOF-5 at higher temperatures (above 400 °C) under an inert atmosphere, thermal decomposition of MOF-5 takes place due to the breaking of carboxylic bridges between  $\text{Zn}_4\text{O}$  cluster and benzene rings of the organic linkers. As reported by Zhang *et al.*, the collapse of frameworks of MOF-5 could follow three types of the partial breaking of carboxylic bridges: (1) Zn-O bond between a carboxylic group and  $\text{Zn}_4\text{O}$  cluster, (2) C-O bond of a carboxylic group and (3) C-C bond between the benzene ring and carboxylic group.[30] Furthermore, the TGA, XRD, FTIR and Raman spectra confirmed this decomposition mechanism where a high wt. % of ZnO (83 % in  $\text{ZnO}/\text{C}_{\text{MOF-5}}$ ) is found in the composites.

The molecular structure of MOF-74 is based on coordinated carboxyl (-COOH) and hydroxy (-OH) groups. Helical Zn-O-C rods are fabricated from 6-coordinated Zn(II) centers, where each Zn has three carboxyl groups. Additionally, there are two doubly bridged hydroxy groups bound. As shown in Fig. 3b, the helical rods (inorganic SBU  $\text{Zn}_3[\text{O}_3(\text{CO}_2)_3]_{\infty}$ ) are linked together via the benzene rings of 2,5-dihydroxybenzene-1,4-dicarboxylate (DHBDC) to form a crystalline 3D honeycomb structure of  $[\text{Zn}_2(\text{C}_8\text{H}_2\text{O}_6)]$  with one-dimensional hexagonal pore channels.[31] Julien *et al.* reported that the decomposition of MOF-74 takes place (above 200 °C) with 50 % weight loss (wt. %) due to the release of  $\text{CO}_x$  species, leaving behind pure ZnO nanoparticles which is in agreement well with our TGA results shown in Fig. 2a.[23] Based on these experimental results, the proposed decomposition mechanism for MOF-74 can be occurred via three types of carboxylic and hydroxyl bond breaking: (1) Zn-O bond between

carboxyl/hydroxyl groups and  $\text{ZnO}_6$  octahedral cluster, (2) C-O bond of carboxyl group and (3) C-C bond between benzene ring and carboxyl/hydroxyl group. Similar to MOF-5, the release of  $\text{CO}_2$  during exothermal decomposition of MOF-74 suggests that the predominantly bond breaking takes place at positions 1 and 3. As confirmed by TGA and XRD results, a significant amount (74.5 wt.%) of well crystalline ZnO nanoparticles enveloped by carbons was formed at 800 °C under water vapors saturated atmosphere with retained morphology, which may suggest that the partial breaking of C-O bonds takes place at position 2 with majority of bonds break at positions 1 and 3.

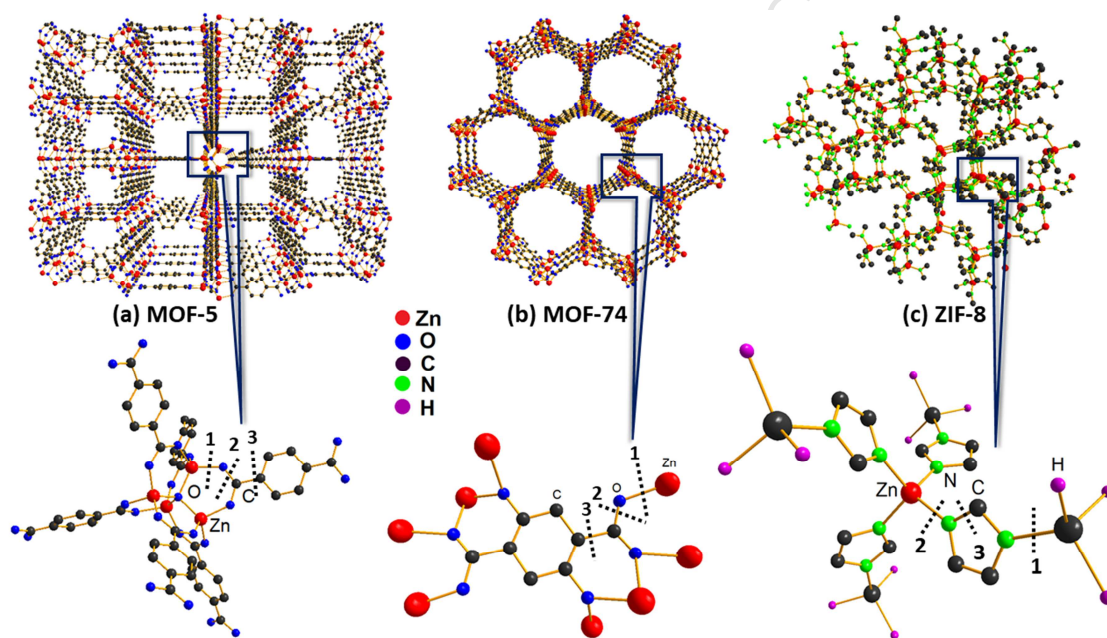


**Fig. 3** The SBUs of Zn ions and organic linkers in crystal structures of (a) MOF-5 (b) MOF-74 and (c) ZIF-8 and the proposed decomposition mechanisms 1, 2 and 3.

Fig. 3c shows the crystal structure of ZIF-8 with sodalite topology. Analogous to zeolites,  $\text{Zn}^{+2}$  ions in ZIF-8 are coordinated to four nitrogen atoms of imidazole ligands forming the  $\text{Zn}(\text{C}_4\text{H}_5\text{N}_2)_2$ . James *et al.* reported that carbonization of ZIF-8 at 300 °C under argon atmosphere leads to the decomposition/disordering of methyl groups and imidazole ring-ring interactions.[32] Xu *et al.* confirmed the decomposition of ZIF-8 under air goes through three steps: 1) displacement of methyl groups around 200 °C without collapse of framework but

thermal expansion is the main change to the ZIF-8 lattice; 2) further thermal expansion and dislodgement of methyl groups above 300 °C, and finally 3) collapse of ZIF-8 framework at temperatures higher than 350 °C, and transformation to ZnO at above 400 °C in air.[33] Based on these observations, three types of bond breakings are possible: (1) CH<sub>3</sub>-C detachment, (2) Zn-N bond, (3) C=N bond of the imidazole ring.[34] These reported results are in good agreement with our experimental results.[21] Compared to composites **ZnO/C<sub>MOF-5</sub>** and **ZnO/C<sub>MOF-74</sub>**, composite **ZnO/C<sub>ZIF-8</sub>** contains relatively low wt. % (35.8 %) of ZnO, which may due to the fact that most of the oxidative interactions occur at methyl substituents of imidazole ligand. Moreover, the lower stoichiometric ZnO nanoparticle formation can be attributed to the deficiency of oxygen and Zn<sup>2+</sup> ions in precursor ZIF-8 [Zn(C<sub>4</sub>H<sub>5</sub>N<sub>2</sub>)<sub>2</sub>]. The TGA, PXRD and XPS results reported here are in good agreement with the previously published reports.[21, 24, 33, 34]

The chemical states and elemental compositions of **ZnO/C<sub>MOF-5</sub>**, **ZnO/C<sub>MOF-74</sub>** and **ZnO/C<sub>ZIF-8</sub>** were investigated by XPS. The elemental survey shows (Fig. 4a) that Zn, O and C in all samples are presented. However, a strong peak of N is observed in **ZnO/C<sub>ZIF-8</sub>** sample. Fig. 4b (highlighted in inset) shows that the intensity of Zn 2p<sub>3/2</sub> peak is lowest in **ZnO/C<sub>ZIF-8</sub>**, moderate in **ZnO<sub>MOF-74</sub>** but highest in **ZnO<sub>MOF-5</sub>**. As confirmed by TGA, it is due to the ZnO content in these samples, **ZnO/C<sub>MOF-5</sub>** > **ZnO/C<sub>MOF-74</sub>** > **ZnO/C<sub>ZIF-8</sub>**. Moreover, the Zn 2p<sub>3/2</sub> peak appeared at 1022.1, 1021.9 and 1021.4 eV for **ZnO/C<sub>MOF-5</sub>**, **ZnO/C<sub>MOF-74</sub>**, and **ZnO/C<sub>ZIF-8</sub>** respectively. This slight difference in Zn 2p<sub>3/2</sub> peaks may be due to the different crystallinity and oxygen-related defects present in ZnO nanoparticles. In **ZnO/C<sub>MOF-5</sub>** and **ZnO/C<sub>MOF-74</sub>** composites carbon is doped in Zn-O crystal lattice creating an energy level above the valence band whereas in **ZnO/C<sub>ZIF-8</sub>** C and N can be co-doped into the Zn-O crystal lattice. The presence of Zn-N bond in **ZnO/C<sub>ZIF-8</sub>** indicates that the N dopants are incorporated at O sites.[24] In all three composites, the binding energy difference between Zn 2p<sub>3/2</sub> and Zn 2p<sub>1/2</sub> is observed 23 eV, confirming the presence of Zn<sup>2+</sup> ions.

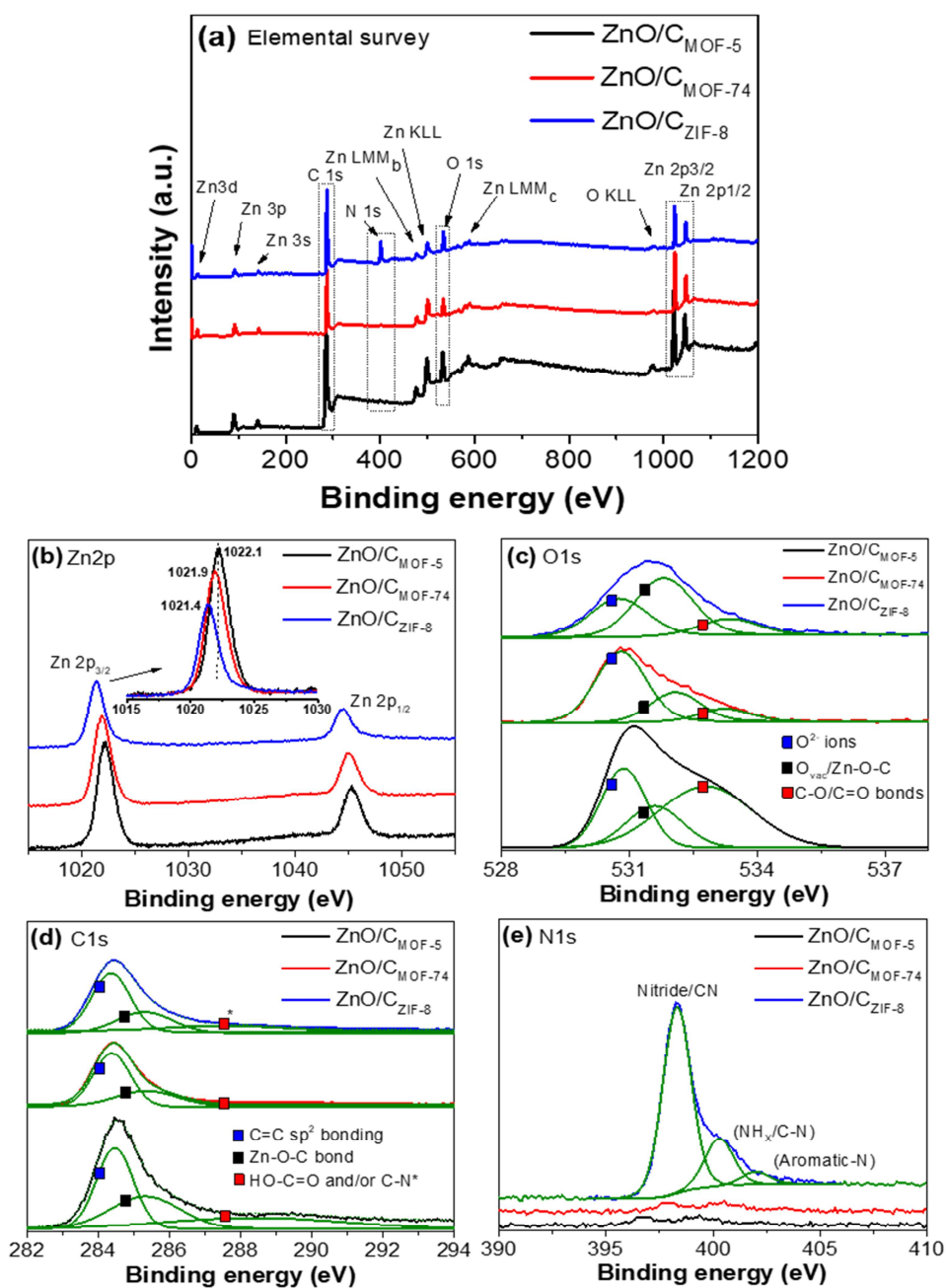


**Fig. 4** XPS spectra of (a) elemental survey (b) Zn 2p (c) O 1s (d) C 1s (e) N 1s for **ZnO/C<sub>MOF-5</sub>** (black) and **ZnO/C<sub>MOF-74</sub>** (red) and **ZnO/C<sub>ZIF-8</sub>** (blue).

It is evident from the XPS spectra of O 1s (Fig. 4c) that the relative intensities of O 1s peaks are in good agreement with Zn 2p<sub>3/2</sub> peaks in **ZnO/C<sub>MOF-5</sub>**, **ZnO/C<sub>MOF-74</sub>**, **ZnO/C<sub>ZIF-8</sub>**.

Upon deconvolution O 1s spectra of **ZnO/C<sub>MOF-5</sub>**, **ZnO/C<sub>MOF-74</sub>** and **ZnO/C<sub>ZIF-8</sub>**, three peaks appear at around 531.2, 531.8 and 533.3 eV. These peaks can be assigned to O<sup>2-</sup> ions of Zn-O bonds, oxygen vacancies (O<sub>vac</sub>) and/or Zn-O-C bonds due to carbon doping into Zn-O lattice and the surface adsorbed hydroxyl (-OH) and carbonate (C-O/C=O) species respectively. Since the XPS peaks of O<sub>vac</sub> and C-dopant are heavily overlapped, it is difficult to distinguish them.[24, 35, 36] The relative intensity of 533.3 eV peak in **ZnO/C<sub>MOF-5</sub>** is higher compared to **ZnO/C<sub>MOF-74</sub>** and **ZnO/C<sub>ZIF-8</sub>**, indicating the higher concentration of carboxyl functional groups (-COOH) attached to the surface of the material, which is also confirmed by FTIR spectra. Additionally, the lower intensity and broader O1s combined with the blue shifted Zn 2p<sub>3/2</sub> peaks of **ZnO/C<sub>ZIF-8</sub>** indicate that nitrogen might be co-doped along with the C-dopant in Zn-O lattice. As shown in Fig. 4e, a high intensity peak of N 1s at 398.3 eV is attributed to O-Zn-N, indicating that N might be incorporated into ZnO nanoparticles at O sites.[24] Two low intensity shoulder peaks at 400.28 and 401.98 eV can be assigned to metal nitride and NO<sub>x</sub> species respectively. No peaks of N 1s were detected in **ZnO/C<sub>MOF-5</sub>** and **ZnO/C<sub>MOF-74</sub>**.

As shown in Fig. 4d, the main C 1s peak in sample **ZnO/C<sub>MOF-5</sub>**, **ZnO/C<sub>MOF-74</sub>** and **ZnO/C<sub>ZIF-8</sub>**, appears at around 284.3 eV, which is assigned to C=C pure graphitic sp<sup>2</sup> bonding. The fitted peak at 285.76 eV in **ZnO/C<sub>MOF-5</sub>** and at 285.35 eV in **ZnO/C<sub>MOF-74</sub>** and **ZnO/C<sub>ZIF-8</sub>** samples corresponds to Zn-O-C bond. A low intensity broader peak positioned at 288.83 eV in **ZnO/C<sub>MOF-5</sub>** is assigned to carboxyl functional groups (O-C=O). This peak showed very low intensity in **ZnO/C<sub>MOF-74</sub>** which indicates that there are less surface adsorbed species present in composites. However, in **ZnO/C<sub>ZIF-8</sub>** a fitted broad peak positioned at 287.5 eV is attributed to C-N/C=O bond.[34, 36] Combined with other characterizations such as TGA and XRD, the XPS analysis results help to find the nature of crystalline structures of MOF derived ZnO/C composites and suggested that the **ZnO/C<sub>MOF-5</sub>** and **ZnO/C<sub>MOF-74</sub>** are C-doped ZnO composites with carboxylic (-COOH) functional groups attached on the surface of the composite. However, the **ZnO/C<sub>ZIF-8</sub>** is an N and C co-doped ZnO/C composite with a negligible amount of carboxyl functional groups attached.

The morphologies of the precursor MOFs and derived ZnO/C composites were investigated by SEM. As shown in Fig. 5, the SEM images clearly confirm that the morphologies of the MOF-5, MOF-74 and ZIF-8 are preserved in **ZnO/C<sub>MOF-5</sub>**, **ZnO/C<sub>MOF-74</sub>** and **ZnO/C<sub>ZIF-8</sub>**

composites derived at 800 °C in water vapors saturated argon. The sizes and shapes of the synthesized precursor MOFs critically depend upon the synthesis parameters. From the SEM images in Fig. 5, the cubic crystals of MOF-5 are in the range of 1  $\mu\text{m}$  whereas the spherical shaped crystals of MOF-74 are around 500 nm. The nanocrystals of ZIF-8 with regular hexagonal shape (confirmed by low magnification TEM) are below 100 nm. As discussed above, carbonization of MOF-5 at high temperature (above 400 °C) in an inert atmosphere causes the partial breaking of Zn-O, C-O and C-C bonds leading to the shrunk crystals with minor cracked surfaces as shown in Fig. 5a and d. Similarly, MOF-74 and ZIF-8 also preserved their morphologies with slightly cracked surfaces shown in Fig. 5e and f respectively. To determine the morphology and structural stability of these MOF derived ZnO/C composites after subject to photocatalytic dye degradation tests, the SEM images of used and dried  $\text{ZnO/C}_{\text{MOF-5}}$ ,  $\text{ZnO/C}_{\text{MOF-74}}$  and  $\text{ZnO/C}_{\text{ZIF-8}}$  samples were also recorded and presented in Fig. S4 a, b and c of Supplementary Data, respectively. It confirms that the morphologies of these ZnO/C composites remain unaffected after photocatalytic dye degradation.

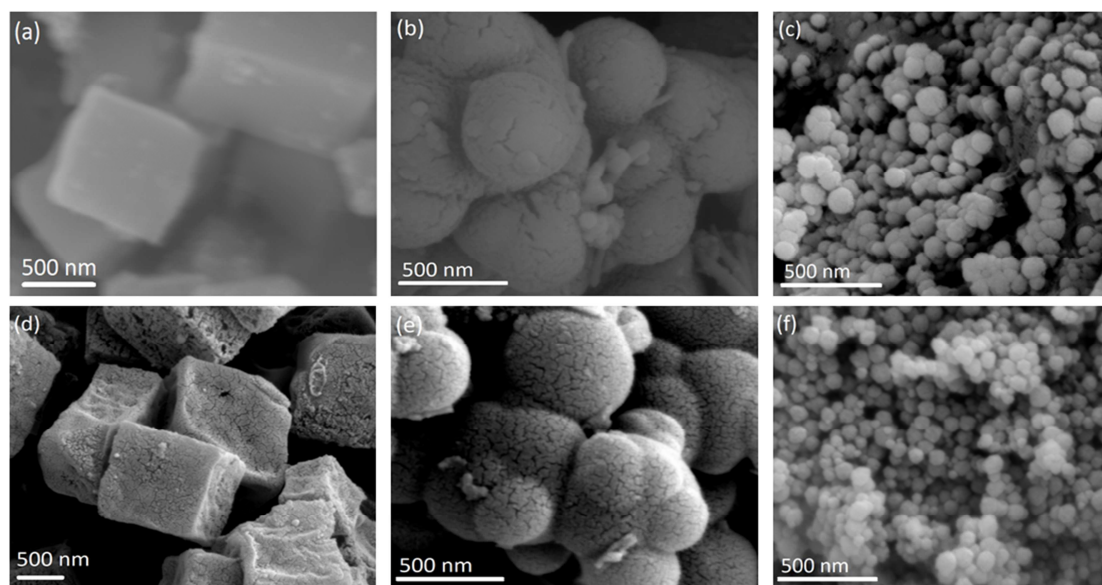


**Fig. 5** SEM micrographs of (a) MOF-5, (b) MOF-74 and (c) ZIF-8 and (d)  $\text{ZnO/C}_{\text{MOF-5}}$ , (e)  $\text{ZnO/C}_{\text{MOF-74}}$  and (f)  $\text{ZnO/C}_{\text{ZIF-8}}$  respectively.

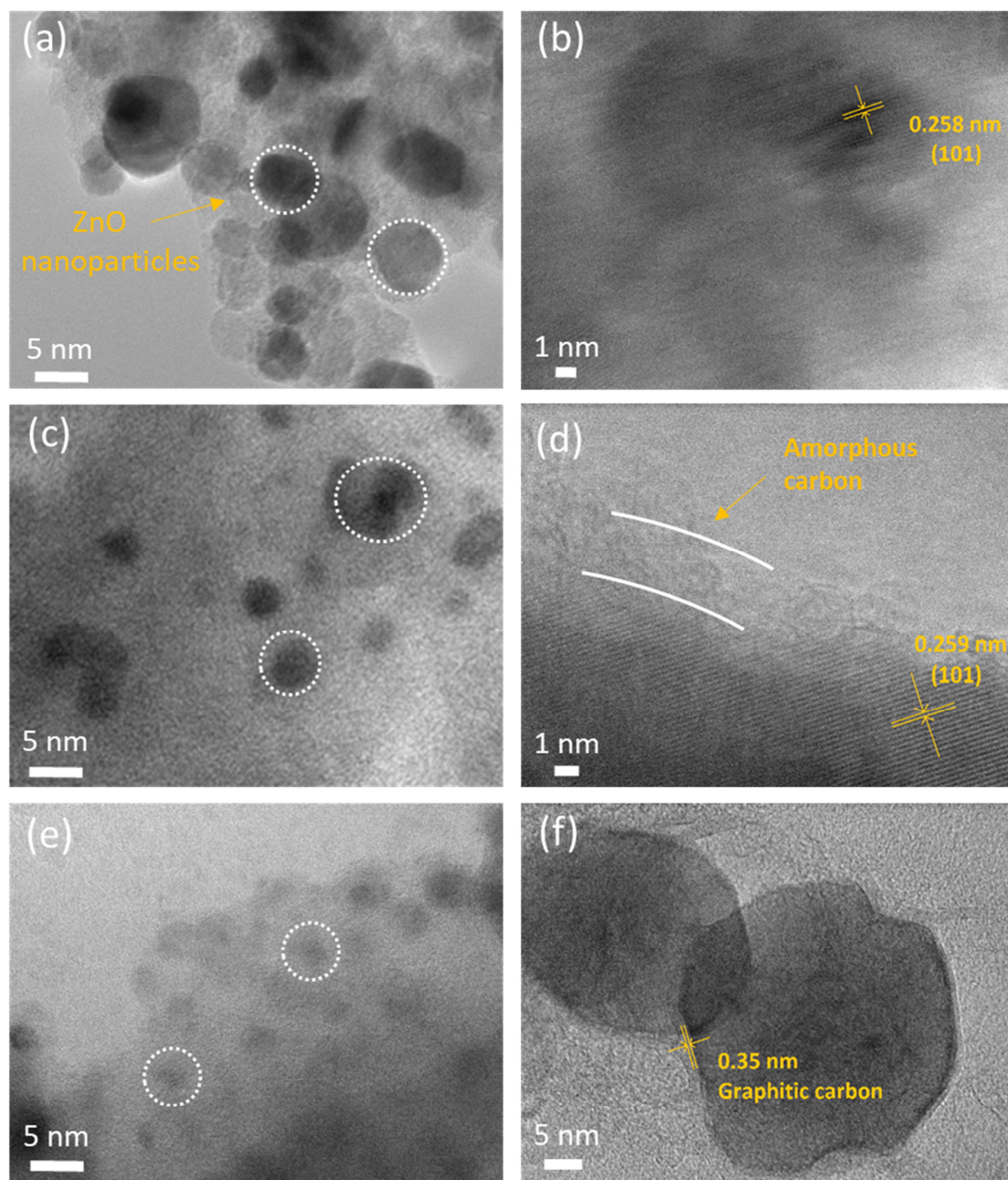


**Fig. 6** HRTEM micrographs of (a, b)  $\text{ZnO}/\text{C}_{\text{MOF-5}}$ , (c, d)  $\text{ZnO}/\text{C}_{\text{MOF-74}}$  and (e, f)  $\text{ZnO}/\text{C}_{\text{ZIF-8}}$ , respectively.

To further investigate the crystal structures and distribution of ZnO in the carbon matrix, TEM and EDX elemental mapping were employed. Fig. 6 shows the TEM images of  $\text{ZnO}/\text{C}_{\text{MOF-}}$

5,  $\text{ZnO}/\text{C}_{\text{MOF-74}}$  and  $\text{ZnO}/\text{C}_{\text{ZIF-8}}$  composites. From Fig. 6a, c and e, it is clear that all three MOFs derivatives exhibit homogeneously distributed ZnO nanoparticles with sizes less than 10 nm embedded in a porous carbon matrix without agglomerations. The d-spacings between the lattice fringes of ZnO in the different ZnO/C composites can be seen from Fig. 6b, d and f respectively. The d-spacing between lattice fringes of (101) for ZnO is 0.258 nm in C doped ZnO/ $\text{C}_{\text{MOF-5}}$  and 0.259 nm in C-doped ZnO/ $\text{C}_{\text{MOF-74}}$  sample, which is obviously larger than that of the (101) for pure ZnO nanoparticles (0.24 nm). The increase in d-spacing between lattice fringes of  $\text{ZnO}/\text{C}_{\text{MOF-5}}$  and  $\text{ZnO}/\text{C}_{\text{MOF-74}}$  suggest the strain on nanoparticles created by the doped C species in these samples.[37] The d-spacing of graphitic carbon fringes in  $\text{ZnO}/\text{C}_{\text{ZIF-8}}$  is 0.35 nm, which confirms the formation of partial graphitic and partial amorphous nature of carbon matrix upon carbonization of MOFs. These findings combined with the results from PXRD and XPS suggest that ZnO nanoparticles in  $\text{ZnO}/\text{C}_{\text{MOF-5}}$  and  $\text{ZnO}/\text{C}_{\text{MOF-74}}$  are well crystalline while only a small amount of poorly crystalline ZnO nanoparticles is preserved in  $\text{ZnO}/\text{C}_{\text{ZIF-8}}$ .

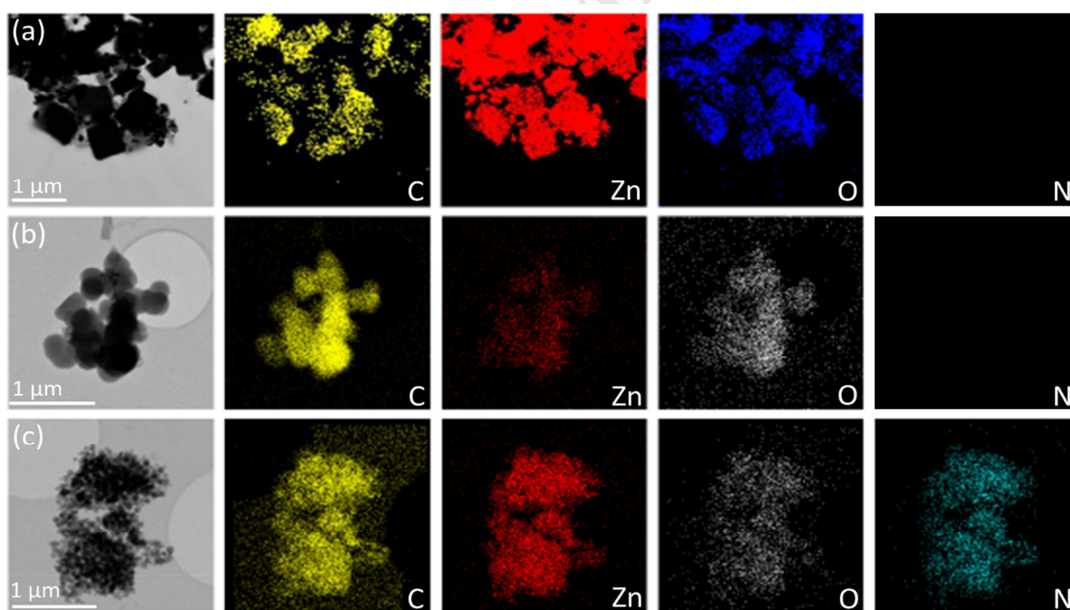


**Fig. 7** Low magnification TEM micrographs and their respective EDX elemental mappings of (a)  $\text{ZnO}/\text{C}_{\text{MOF-5}}$ , (b)  $\text{ZnO}/\text{C}_{\text{MOF-74}}$  and (c)  $\text{ZnO}/\text{C}_{\text{ZIF-8}}$ . The colored images show the distribution of elements throughout the composites. C, Zn, and O and N are represented in yellow, red, blue/gray and cyan respectively.

Fig. 7a, b and c represent the energy dispersive X-ray spectroscopy (EDX) element mapping of **ZnO/C<sub>MOF-5</sub>**, **ZnO/C<sub>MOF-74</sub>** and **ZnO/C<sub>ZIF-8</sub>** composites respectively. The elemental maps of C, Zn and O for all the 3 composites exhibit similar patterns to their TEM images. Additionally, N is uniformly presented in sample **ZnO/C<sub>ZIF-8</sub>**. The TEM and EDX results are in good agreement with XPS results, which evidently demonstrate that the homogeneously distributed ZnO nanoparticles and C and/or N species on the composite samples obtained from precursor MOFs. This may be due to the fact that the MOFs are robust molecule-like crystal structures with good thermal stability.

To investigate the allotropic forms of carbon and functional groups attached to the surfaces of the derived **ZnO/C<sub>MOF-5</sub>**, **ZnO/C<sub>MOF-74</sub>** and **ZnO/C<sub>ZIF-8</sub>** composites, Raman and FTIR spectra were recorded. The main Raman peaks of ZnO nanoparticles (Fig. 8) appeared at 427.3 and 320.1  $\text{cm}^{-1}$  in **ZnO/C<sub>MOF-5</sub>** which correspond to  $E_2(\text{high})$  and  $A_1(\text{TO})$  vibrational modes respectively. The bulk ZnO exhibits  $E_2(\text{high})$  mode at 437  $\text{cm}^{-1}$ . However, in **ZnO/C<sub>MOF-74</sub>** and **ZnO/C<sub>ZIF-8</sub>**,  $E_2(\text{high})$  mode appears at 428.4 and 431.7  $\text{cm}^{-1}$  while  $A_1(\text{TO})$  mode appeared at 321.2  $\text{cm}^{-1}$  respectively. The low intensity of ZnO peaks in **ZnO/C<sub>ZIF-8</sub>** also confirms the poor crystallinity and low wt. % of ZnO nanoparticles observed in PXRD. Moreover, the appearance of  $E_2(\text{high})$  vibrational mode at a different frequency in **ZnO/C<sub>ZIF-8</sub>** might be due to the dissimilar doping profile as compared to **ZnO/C<sub>MOF-5</sub>** and **ZnO/C<sub>MOF-74</sub>**. [37] The significant red-shift indicates the reduced particle sizes compared to the bulk ZnO and the narrowing of energy band gap due to C and/or N doping in ZnO. The doped C and N atoms may cause a strain which modifies the lattice parameters of ZnO and creates  $O_{\text{vac}}$  related crystalline defects. Another interesting observation is that sample **ZnO/C<sub>ZIF-8</sub>** shows new peaks at 271 and 574  $\text{cm}^{-1}$ , which are not observed in pure ZnO. Numerous reports suggested that these additional peaks come from the activated silent modes  $B_1(\text{low})$  and  $B_1(\text{high})$  respectively. These modes appear due to the different electronic properties of doped N and the substituted O in ZnO. [38-42] It can be clearly seen (inset in Fig. 8) that  $B_1(\text{low})$  and  $B_1(\text{high})$  modes are also not observed in **ZnO/C<sub>MOF-5</sub>** and **ZnO/C<sub>MOF-74</sub>**. Furthermore, the  $E_2(\text{M})$  multi-phonon vibrational modes appearing at 320.1  $\text{cm}^{-1}$  are much stronger in **ZnO/C<sub>MOF-5</sub>** and **ZnO/C<sub>MOF-74</sub>** compared to **ZnO/C<sub>ZIF-8</sub>**. This  $E_2(\text{M})$  multi-phonon mode in ZnO nanoparticles is commonly attributed to the

defects and impurities caused by the C doped species.[43] In pure ZnO, this mode is negligible. As confirmed by UV-Vis absorption spectra, doping of N creates a new energy level above the valence band. It is evident that C acts as a dopant in MOF-5 and MOF-74 derived ZnO/C composites whereas in ZIF-8 derived ZnO/C composites, N is the primary dopant.[21, 24] It can be therefore concluded that compared to bulk ZnO, the red-shift of modes towards lower frequencies in all these MOF-derived ZnO/C composites could be an indirect validation of the reduced particle sizes and the narrowed energy band gaps, which is also confirmed by HRTEM (Fig. 6) and UV-Vis absorption spectroscopy (Fig. 9).

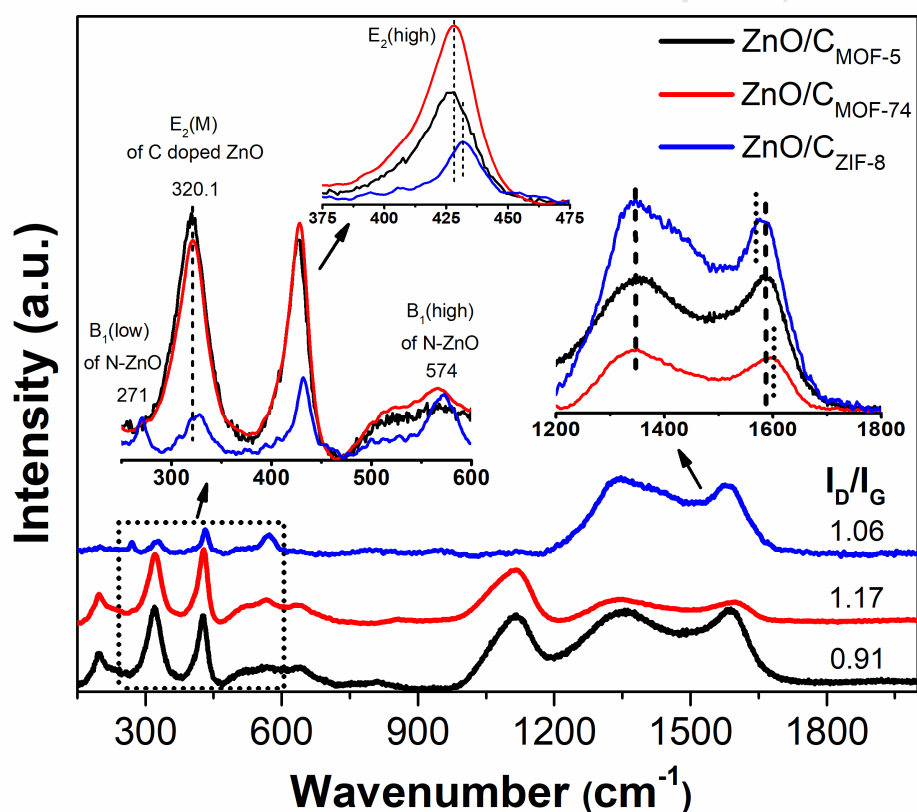


**Fig. 8** Raman spectra of  $\text{ZnO/C}_{\text{MOF-5}}$ ,  $\text{ZnO/C}_{\text{MOF-74}}$  and  $\text{ZnO/C}_{\text{ZIF-8}}$  are presented in black, red and blue respectively. Insets show the highlighted main  $E_2(\text{high})$  and  $E_2(\text{M})$  modes of ZnO, additional modes ( $B_1$ ) as well as D and G bands of amorphous carbon.

The two signature peaks of D and G bands of amorphous carbon at around 1350 and 1580  $\text{cm}^{-1}$  are observed in all the composites. The D band at around 1350  $\text{cm}^{-1}$  in Raman spectra

represents the breathing modes of  $sp^2$  hybridized carbon atoms in hexagonal carbon rings and signifies the (diamond-like  $sp^3$  C-C bonds) amorphization of carbon. The G band appeared at around  $1580\text{-}1600\text{ cm}^{-1}$  is due to the in-plane bond stretching of all  $sp^2$  bonded atoms in hexagonal carbon rings and chains. The intensity ratio of D and G bands ( $I_D/I_G$ ) is analogous to the  $sp^3/sp^2$  ratio which is a measure of amorphization of carbon.[24] In our samples, these Raman peaks of D and G bands for samples **ZnO/C<sub>MOF-5</sub>**, **ZnO/C<sub>MOF-74</sub>** and **ZnO/C<sub>ZIF-8</sub>** appear at a slightly different position with calculated  $I_D/I_G$  ratios of 0.91, 1.17 and 1.06 respectively. It suggests that the decomposition of the organic linker ( $C_8H_6O_4$ ) in MOF-5 at high temperature leads to partial collapse of framework due to the breaking of C-O and C-C bonds and give relatively more graphitic carbon compared to the MOF-74 and ZIF-8 derived composites. During the carbonization of ZIF-8 under water vapors saturated argon, the framework collapses by the disintegration of organic linker methylimidazole ( $C_4N_2H_6$ ) which is formed due to the partial breaking of Zn-N and C=N bonds. The high content of nitrogen presented on the carbon surface increases the  $sp^3$  hybridized C-C bonds, as confirmed by XPS (Fig. 4e), which enhances the intensity of the D band. The shift of G band position to  $1599\text{ cm}^{-1}$  in **ZnO/C<sub>MOF-74</sub>** can presumably be due to the indirect influence of  $sp^3$  content. In their study on disordered and amorphous carbon, Ferrari *et al.* argued that the creation of defects, bond length disorder and  $sp^2/sp^3$  hybridization play the critical role in amorphization of carbon. During the conversion of graphite to nanocrystalline carbon, G band moves from  $1581\text{ cm}^{-1}$  to  $1600\text{ cm}^{-1}$ ,  $sp^3$  bonding grows and  $I_D/I_G$  ratio increases.[44] Based on these observations, it can be expected that the decomposition of the organic linker ( $C_8H_2O_6$ ) and breakdown of the spherically arranged framework of MOF-74 leads to relatively high amorphous carbon.

FTIR spectra of **ZnO/C<sub>MOF-5</sub>**, **ZnO/C<sub>MOF-74</sub>** and **ZnO/C<sub>ZIF-8</sub>** composites derived in water vapors saturated argon atmosphere (Fig. S5a in Supplementary Data) exhibit peaks of Zn-O stretching at  $459\text{ cm}^{-1}$ . However, very low intensity of this peak observed in **ZnO/C<sub>ZIF-8</sub>** is in good agreement with XRD (Fig. 2) and Raman results (Fig. 8). Two strong peaks at  $1629$  and  $1047\text{ cm}^{-1}$  in **ZnO/C<sub>MOF-5</sub>** correspond to the bond stretching of carboxyl ( $O=C-OH$ ) and C-O/C-OH functional groups on the surfaces of the composite respectively. The weak intensity of this peak in **ZnO/C<sub>MOF-74</sub>** and **ZnO/C<sub>ZIF-8</sub>** indicates the low concentration of C-O bonds presented in these composites.[45] However, a pair of prominent peaks at around  $2850$  and  $2911\text{ cm}^{-1}$  appears in **ZnO/C<sub>MOF-74</sub>** and **ZnO/C<sub>ZIF-8</sub>** composites which can be assigned to the symmetric and

asymmetric stretching modes of  $sp^3$  bonded C-H atoms respectively. As shown in Raman results, the D band is stronger in these samples than in **ZnO/C<sub>MOF-5</sub>**, which also endorses the amorphous nature of the carbon. To determine whether the photocatalytic degradation of MB can affect the surface chemistry of the tested composites, FTIR spectra of MB and used samples were recorded. As shown in Fig. S5b, no peaks of MB were observed in **ZnO/C<sub>MOF-5</sub>**, **ZnO/C<sub>MOF-74</sub>** and **ZnO/C<sub>ZIF-8</sub>** after the photocatalytic dye degradation, suggesting the surface functionalities of the composites remain unaffected.

The optical properties and energy band gaps of the derived ZnO/C composites were calculated from UV-Vis absorption spectra. As shown in Fig. 9a, the UV-Vis absorption spectra of **ZnO/C<sub>MOF-5</sub>**, **ZnO/C<sub>MOF-74</sub>** and **ZnO/C<sub>ZIF-8</sub>** red-shifts from 367 nm for bulk ZnO to 401, 404 and 431 nm respectively. The energy band gaps (EBG) of these composites calculated (Tauc plots) appear at 3.13, 3.11 and 2.97 eV respectively. The redshift in EBGs can be assigned to the defect generation related to  $O_{vac}$  and C and/or N doping into the ZnO nanoparticles.[35] It is found that regardless of different primary anionic dopants in these composites (C for MOF-5 and MOF-74 derived composites and N for ZIF-8 derived composites), the shift in energy band gap is in general not very large with respect to each other. The relatively larger shift in EBG of **ZnO/C<sub>ZIF-8</sub>** may be due to the fact that the released N atoms during the decomposition of methylimidazole organic linkers at high temperature are predominately attached to the surface of carbon which result in the increase of the D band (Raman spectra), accompanied with a small amount of N atoms co-doped into the ZnO with C that result in the narrowing of the EBG.[21, 24] This observation is in good agreement with results from Raman ( $B_1$ (low) and  $B_1$ (high) modes) and XPS spectra. However, it is expected that due to the decrease of energy band gaps in all the three composites compared to the commercially available bulk ZnO with band gap 3.37 eV, these homogeneously distributed ZnO nanoparticles in porous carbon matrices may potentially absorb more visible light, which can consequently result in improved photocatalytic performance.

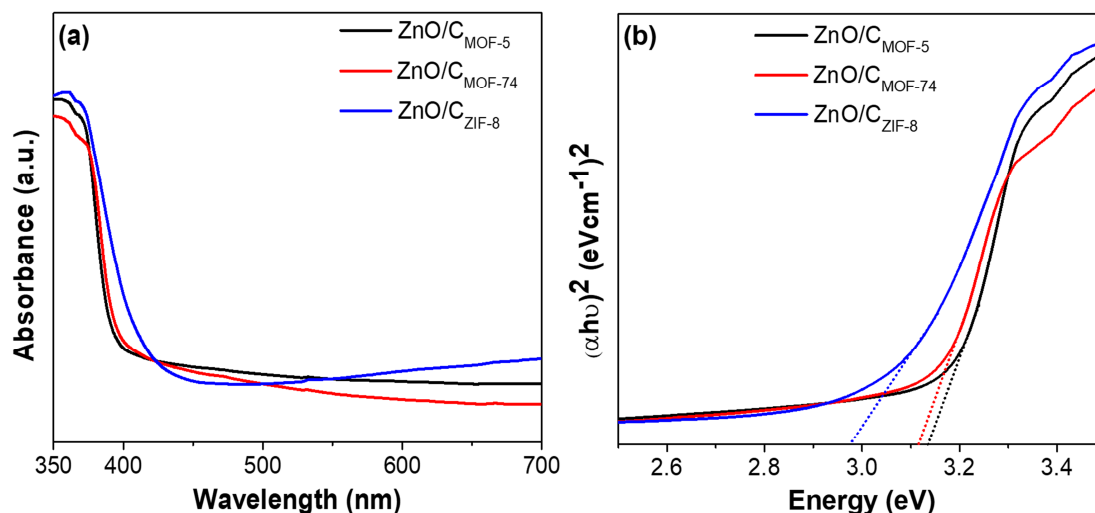


**Fig. 9** (a) UV-vis absorption spectra of **ZnO/C<sub>MOF-5</sub>** (black), **ZnO/C<sub>MOF-74</sub>** (red) and **ZnO/C<sub>ZIF-8</sub>** (blue) and (b) direct energy band gaps (Tauc plots) of the composites.

Specific surface areas and pore sizes of ZnO/C nanocomposites play an important role in adsorption and eventually photodegradation of organic dyes. Fig. 10 shows the N<sub>2</sub> sorption isotherms at 77K for all the three composites. The measured BET surface areas of **ZnO/C<sub>MOF-5</sub>**, **ZnO/C<sub>MOF-74</sub>** and **ZnO/C<sub>ZIF-8</sub>** are 390, 321 and 653 m<sup>2</sup> g<sup>-1</sup>, respectively. The qualitative behavior of isotherms shows that **ZnO/C<sub>MOF-5</sub>** displays type-II isotherm with hysteresis at higher relative pressure (in the presence of micro/mesopores), while both **ZnO/C<sub>MOF-74</sub>** and **ZnO/C<sub>ZIF-8</sub>** exhibit type-I isotherms with very small hysteresis at relative pressure ( $p/p_0$ ) between 0.4 - 0.6, indicating the dominance of micropores with small volume of mesopores.[45-47] It is fascinating to see that the crystal structures and pore shapes of the precursor MOFs remain preserved with the creation of micro-cracks during carbonization process (confirmed by SEM and TEM), depending upon the calcination temperature and gaseous atmosphere.

The pores size distributions (PSD) (inset in Fig. 10) were calculated by NLDFT method. It can be seen that high N<sub>2</sub> uptake at lower pressures ( $p/p_0$ ) and linear isotherms (with very small hysteresis loop) demonstrate that micropores are predominated in **ZnO/C<sub>ZIF-8</sub>** with pore widths centered at 1.2 and 1.6 nm. However, a small fraction of hierarchical mesopores between 2 and 3.5 nm are also observed. Similarly, **ZnO/C<sub>MOF-74</sub>** is dominated with micropores centered at size of 1.6 nm with a shoulder micropore size at 1.2 nm. However, **ZnO/C<sub>MOF-5</sub>** exhibited major

micropore size at 1.4 nm with a shoulder pore size at 1.7 nm. Additionally, a wide band of hierarchical mesopores between 2.2 and 5 nm are observed in this sample due to the voids between particles.

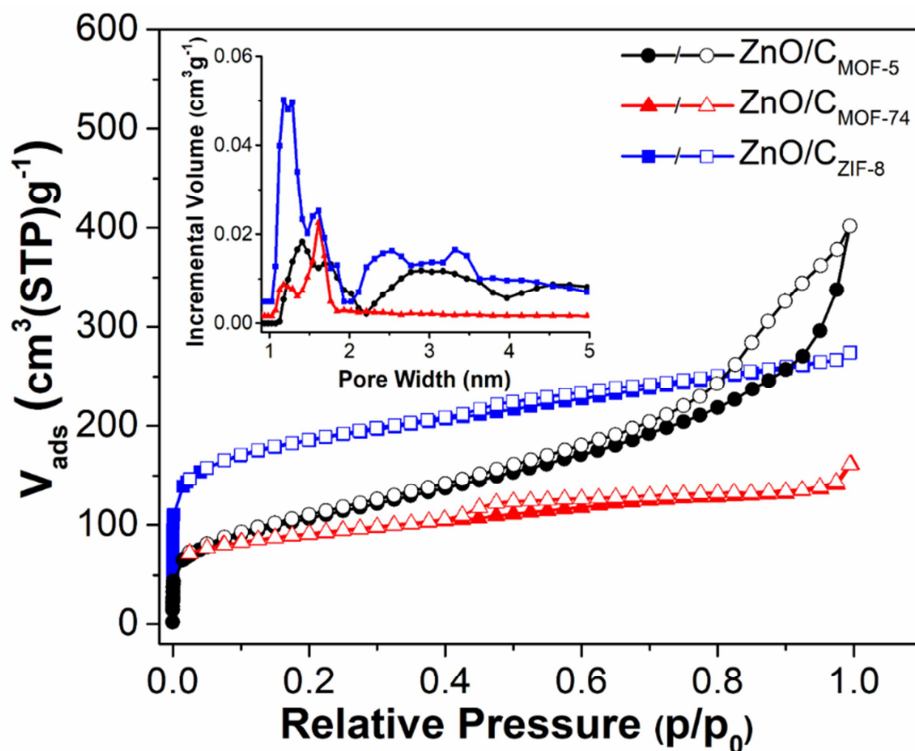


**Fig. 10**  $\text{N}_2$  sorption isotherms measured at 77 K for  $\text{ZnO}/\text{C}_{\text{MOF-5}}$  (black circles),  $\text{ZnO}/\text{C}_{\text{MOF-74}}$  (red triangles) and  $\text{ZnO}/\text{C}_{\text{ZIF-8}}$  (blue squares). The inset is the pore size distributions of MOF derived  $\text{ZnO}/\text{C}_{\text{MOF-5}}$ ,  $\text{ZnO}/\text{C}_{\text{MOF-74}}$  and  $\text{ZnO}/\text{C}_{\text{ZIF-8}}$  nanocomposites.

The relationship between pore shapes/sizes of precursor MOF and their derived ZnO/C can be understood by linking the PSD of derived composites with their precursor frameworks. The  $\text{N}_2$  sorption isotherms and PSDs of derived ZnO/C composites of MOF-5, MOF-74 and ZIF-8 are in good agreement with pore structures of precursor MOFs. As discussed above and shown in Fig. 3a, MOF-5, a simple cubic framework consisting of  $\text{Zn}_4\text{O}$  nodes and benzene-dicarboxylate linkers, predominantly possesses an open pore structure, which can allow the small molecules to diffuse into the pores.[34, 35] The incremental pore volume (inset in Fig. 10) shows that after carbonization at 800 °C under water vapors saturated argon atmosphere, the organic

ligand decomposes and leads to the creation of slightly larger micropores and mesopores. The breakings of Zn-O, C-O and C-C bonds in MOF structure result in partial migration and clustering of Zn atoms from metal centers to the pore cavities. Due to the collapse of the node-ligand structure, the consequent decomposition of the organic linkers and the migration of Zn species, these pore cavities are randomly blocked, resulting in the decrease in specific surface areas and the increase in pore sizes of the derivatives relative to their precursors.[23, 30, 32]

Similarly, Zn-N<sub>4</sub> tetrahedra in ZIF-8 are linked through methylimidazole rings forming spherical hexagonal structures with pore size closer to MOF-5. However, ZnN<sub>4</sub>-imidazole linked in spherical order (Fig. 3c) creates more pore openings with a size smaller than that of the cubic shaped MOF-5.[30, 32] Compared to **ZnO/C<sub>MOF-5</sub>** and **ZnO/C<sub>MOF-74</sub>**, composite **ZnO/C<sub>ZIF-8</sub>** exhibits higher micropore volume and specific surface area. It is in good agreement with TGA and XRD results that among these composites discussed here, **ZnO/C<sub>ZIF-8</sub>** possesses the least amount of ZnO nanoparticles (35.8 wt. %) upon carbonization of ZIF-8 at 800 °C in water vapors saturated argon atmosphere, which results in high amount (wt. %) of microporous carbon in **ZnO/C<sub>ZIF-8</sub>** with increased specific surface area (653 m<sup>2</sup> g<sup>-1</sup>), but preserving the N-doped microporous carbon framework as confirmed by SEM and TEM images.[25]

As mentioned above, the pore shapes of MOF-74 are different with respect to MOF-5 and ZIF-8. Instead of possessing enclosed pores, it consists of long cylindrical channels with 1-D hexagonal where metal nodes form the stripes down the channel length as shown in Fig. 3b.[48, 49] The narrow pore distribution and the relatively low specific surface area of **ZnO/C<sub>MOF-74</sub>** (321 m<sup>2</sup> g<sup>-1</sup>) as compared to **ZnO/C<sub>MOF-5</sub>** and **ZnO/C<sub>ZIF-8</sub>**, are related to the lower specific surface area of precursor MOF-74 and its densely packed molecular structure. However, the specific surface area of **ZnO/C<sub>MOF-74</sub>** is much lower than that of **ZnO/C<sub>MOF-5</sub>** and **ZnO/C<sub>ZIF-8</sub>**. It can be assumed that the 1-D cylindrical pore structure of MOF-74 does not provide enough path lengths for ZnO nanoparticles to migrate to the cavities upon breaking of C-O, Zn-O bonds and collapse the framework, which results in narrow pore size distribution (predominant micropores) and relatively less decreased surface area.

### 3.2 Photocatalytic performances of the ZnO/C composites

To study the photocatalytic properties of **ZnO/C<sub>MOF-5</sub>**, **ZnO/C<sub>MOF-74</sub>** and **ZnO/C<sub>ZIF-8</sub>**, these composites were tested for photocatalytic dye degradation of methylene blue (MB) and

hydrogen ( $H_2$ ) evolution under visible light. The proposed mechanism of photocatalytic dye degradation and  $H_2$  evolution are shown in Fig. 11. When the visible light has energy equivalent to or higher than the energy band gap of ZnO, the energy of visible light is absorbed by the ZnO nanoparticles, the valence band electrons are excited generating electron-hole ( $e^-/h^+$ ) pairs. These photo-generated holes can directly oxidize MB into neutral species. Moreover, these photo-generated holes can also react with water molecules (since the reaction takes place in water) and produce hydroxyl radicals ( $OH^\bullet$ ). Simultaneously, photo-generated electrons in conduction band reduce the oxygen molecules ( $O_2$ ) to form superoxide ions ( $^{\bullet}O_2^-$ ). In conventional metal oxide photocatalysts, the recombination of photo-generated  $e^-_{CB}$  and  $h^+_{VB}$  can take place on the surface of the catalyst, which results in a drastic decrease of photocatalytic activity. In addition, the metal oxides have high surface energies which tend to agglomerate, therefore providing less access to the photocatalytic active sites. However, in MOF derived composites, metal oxides are uniformly distributed in a porous carbon matrix. Due to their high surface areas and appropriate pore sizes, these composites can adsorb higher amount of MB molecules. These adsorbed MB molecules have better access to the photocatalytic active sites on metal oxide. As shown in Fig. 11, the photo-generated electrons in conduction band can be transferred to the carbon matrix which facilitates charge separation by extending the lifetime of photo-excited charge carriers, consequently the possibilities of charge recombination are also minimized. The superoxide radicals ( $^{\bullet}O_2^-$ ) produced by  $e^-_{CB}$  reduce the adsorbed MB into harmless species. On the valence band, photo-generated  $h^+_{VB}$  and  $OH^\bullet$  radicals oxidize the MB molecules and convert them into neutral species. Some recent studies used electron spin resonance (ESR) and species trapping experiment results to describe the mechanism of photocatalytic degradation and complete mineralization of organic dyes by MOF derived carbon doped ZnO composites.[50]

For the photocatalytic hydrogen evolution reaction (HER) under visible light, 35 %  $H_2O/MeOH$  solution was used. The excited electrons in the conduction band react with  $H_2O/MeOH$  solution and reduce the  $H^+$  ions into  $H_2$  gas. To achieve  $H_2$  evolution through photocatalytic water splitting, the conduction band of semiconductor should be more negative than the reduction potential of  $H^+/H_2O$  (0 V vs NHE) and the valence band should be more positive than the oxidation potential of  $H_2O/O_2$  (1.23 V vs NHE).[51] Consequently, the minimum energy required to drive the reaction is 1.23 eV. MOF derived ZnO/C composites have energy band gaps around 3 eV, the incident visible light can therefore easily generate excessive

$e^-/h^+$  pairs to carry out the photocatalytic water splitting. When visible light is shone on MOF derived ZnO/C composites, excitons  $e^-_{CB}/h^+_{VB}$  are generated by the absorbed photons (as shown in Fig. 11) in conduction band (CB) and valance band (VB) of ZnO nanoparticles respectively. These photo-generated  $e^-_{CB}$  and  $h^+_{VB}$  go through a relaxation in CB and VB respectively. Followed by  $e^-_{CB}$  and  $h^+_{VB}$  are separated by overcoming exciton binding energy, the electronic structure of the semiconductor guides the charge diffusion and charge transfer to the respective reaction sites, where the effective charge diffusion and charge transport usually take place very fast. The interfacial surfaces of ZnO and C in MOF derived composites may facilitate successful charge transport by minimizing the possible charge recombination. The photo-generated  $h^+_{VB}$  (as well as  $OH^\bullet$  radicals produced from  $H_2O$ ) react with MeOH used as a hole/radical scavenger to complete the other half-reaction.[52]

For dye degradation, 10 mg of as-synthesized sample was added into 50 mL of 20 ppm MB solution on constant stirring and put under visible light. As shown in Fig. 12a, all three nanocomposites exhibited excellent adsorption and photocatalytic dye degradation. In 6 hours, the nanocomposites **ZnO/C<sub>MOF-5</sub>**, **ZnO/C<sub>MOF-74</sub>** and **ZnO/C<sub>ZIF-8</sub>** showed 99 %, 92 % and 94 % dye degradation respectively. To confirm that if any self-sensitization of MB takes place, pure MB was put under visible light for 6 hours. No self-degradation of MB is observed. Obviously, the MB is stable in visible light under the used conditions to carry out the experiment. Moreover, as-prepared pure ZnO nanoparticles from calcination of MOF-5 at 800 °C in air (named **ZnO<sub>Air</sub>**) was tested as a control experiment following the same photodegradation procedure. After 6 hours, only 26% MB was photodegraded on pure ZnO. Therefore, it can be established that C and N dopants as well as porous carbon matrices derived from the carbonization of MOFs, play an extremely important role in photocatalytic performance of MB degradation.

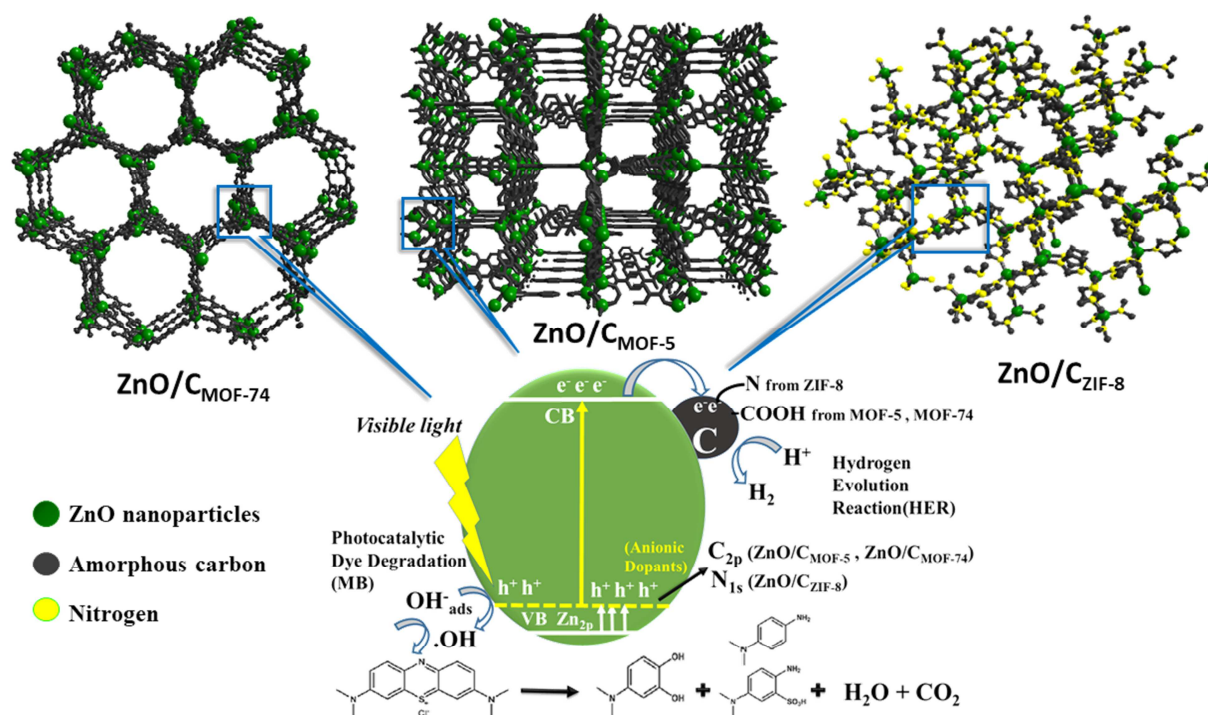


**Fig. 11** Proposed mechanisms of photocatalytic hydrogen evolution reaction (HER) and the photodegradation of organic pollutant dye methylene blue (MB) by  $\text{ZnO}/\text{C}_{\text{MOF-5}}$ ,  $\text{ZnO}/\text{C}_{\text{MOF-74}}$  and  $\text{ZnO}/\text{C}_{\text{ZIF-8}}$  under visible light. The photocatalytic oxidation (degradation of MB) takes place through the photo-generated holes ( $h^+_{\text{VB}}$  and  $\text{OH}^\bullet$  radicals) in valance band (half reaction is shown here) whereas the reduction ( $\text{H}_2$  evolution) occurs through the photo-generated electrons ( $e^-_{\text{CB}}$ ) in the conduction band (half reaction is shown here).

In photocatalytic dye degradation, adsorption of dye on the catalyst and the subsequent photodegradation take place simultaneously. To distinguish these two simultaneous processes, the photocatalytic experiment was carried out in dark. As shown in Fig. S6,  $\text{ZnO}/\text{C}_{\text{MOF-5}}$ ,  $\text{ZnO}/\text{C}_{\text{MOF-74}}$  and  $\text{ZnO}/\text{C}_{\text{ZIF-8}}$  adsorbed 54, 23 and 40 % of MB respectively in 4 hours. The relatively higher adsorption in  $\text{ZnO}/\text{C}_{\text{MOF-5}}$  can be due to the  $-\text{COOH}$  functional groups attached on the surface of amorphous carbon (confirmed by FTIR) which increase the hydrophilicity of the adsorbents. The presence of relatively higher amount of mesopores in  $\text{ZnO}/\text{C}_{\text{MOF-5}}$  and  $\text{ZnO}/\text{C}_{\text{ZIF-8}}$  composite (as shown the PSD in the inset to Fig. 10) also enables the MB molecules have better access to and penetrate into the pores, leading to enhanced adsorption capacity. This

observation is in good agreement with our previously reported results.[21, 22] Contrary to that, the poor adsorption of MB on  $\text{ZnO}/\text{C}_{\text{MOF-74}}$  after 60 minutes could be due to the narrow 1D pore channels of carbon matrix which appear less accessible for the MB molecules to penetrate. Therefore, most of the adsorption takes place on the surface of the catalyst.

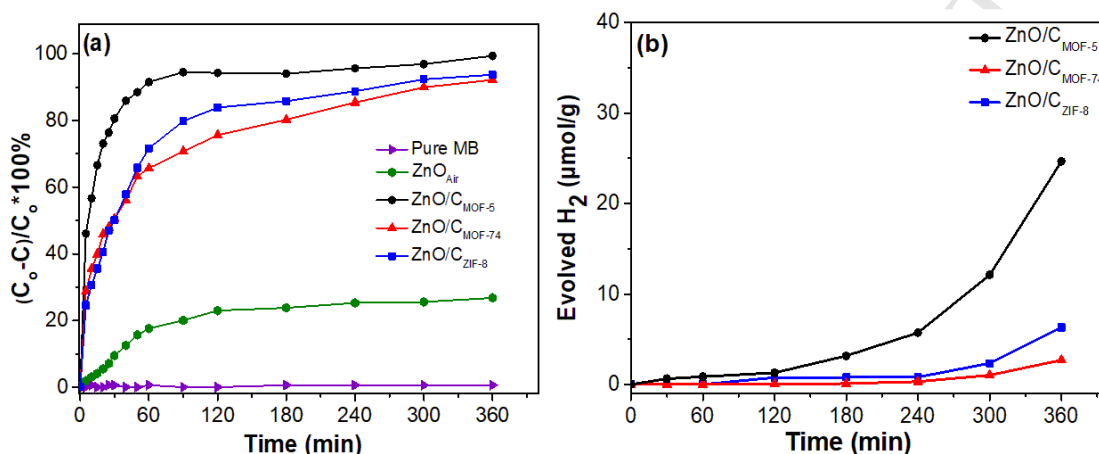


**Fig. 12** (a) The adsorption and photodegradation of MB by  $\text{ZnO}/\text{C}_{\text{MOF-5}}$  (black circles),  $\text{ZnO}/\text{C}_{\text{MOF-74}}$  (red triangles) and  $\text{ZnO}/\text{C}_{\text{ZIF-8}}$  (blue squares) under visible light irradiation respectively.  $\text{ZnO}_{\text{MOF-5}}$  (olive hexagons) is photodegradation by samples prepared at 800 °C under air atmosphere. Violet triangles represent the blind test of MB without any catalysts. (b)  $\text{H}_2$  evolution (HER) reaction by  $\text{ZnO}/\text{C}_{\text{MOF-5}}$ ,  $\text{ZnO}/\text{C}_{\text{MOF-74}}$  and  $\text{ZnO}/\text{C}_{\text{ZIF-8}}$  nanocomposites under visible light irradiation.

Under the visible light,  $\text{ZnO}/\text{C}_{\text{MOF-5}}$  adsorbed and photodegraded 91 % MB while  $\text{ZnO}/\text{C}_{\text{MOF-74}}$  and  $\text{ZnO}/\text{C}_{\text{ZIF-8}}$  showed 65 and 70 % adsorption and photodegradation in the first 60 minutes respectively. Among these samples, fast adsorption and photodegradation of MB on composite  $\text{ZnO}/\text{C}_{\text{MOF-5}}$  could be due to its relatively larger pore widths and the presence of micro/mesopores (as shown in Fig. 10) which allow the dye molecules to penetrate and access active sites deep in the porous carbon matrix. The high content of ZnO (83 wt. %) nanoparticles in this sample may provide accessible active sites due to the exposed metal oxide surfaces. It favors the short diffusion lengths for the charge transport and less charge recombination. Moreover, carboxyl ( $-\text{COOH}$ ) functional groups (confirmed by XPS and FTIR) attached to the

surface of the catalyst may act as trapping centers to also increase the possibilities of adsorption and photodegradation.

Although **ZnO/C<sub>ZIF-8</sub>** has the highest specific surface area with nitrogen decorated carbon matrix among these samples, it exhibited moderate adsorption and photodegradation performance in first 60 min, which may be due to the smaller pore openings as well as less amount of ZnO (35.8 wt. %) present in the composite. While the composite **ZnO/C<sub>MOF-74</sub>** showed slow adsorption in the first 60 minutes as compared to **ZnO/C<sub>MOF-5</sub>**, which might be due to the 1-D pore structure and relatively low specific surface area of **ZnO/C<sub>MOF-74</sub>**. However, after 60 min, it showed the highest degradation performance of MB among all the samples. The overall dye degradation performance in 6 hours is almost the same as **ZnO/C<sub>MOF-5</sub>** and **ZnO/C<sub>ZIF-8</sub>**. It can be presumed that **ZnO/C<sub>MOF-74</sub>** with higher wt. % of ZnO nanoparticles (74.5 %) has more exposed chain-like metal sites that can cause higher photodegradation after 60 min. These observations indicate that the photocatalytic dye degradation is a complicated process depending upon many physical parameters including energy band gaps, ZnO and C ratios in the nanocomposites, specific surface areas, pore width and pore volume of the composites, crystallinity and functional groups attached on the surface, which are consistent with the previous report.[22] In Table 1, a comparison of photocatalytic MB degradation efficiencies of ZnO and doped ZnO under visible light is provided. Obviously, ZnO/C composites derived from MOF precursors are amongst the best performance materials in the photodegradation of MB under visible light irradiation.

The porous carbon matrix in ZnO/C composites not only adsorbs dyes but may also play a role in the degradation of MB. Therefore, it is difficult to distinguish the contribution of this simultaneously occurring adsorption and photodegradation of organic dyes using UV-Vis spectroscopy. To investigate the photodegradation of MB by MOF derived C and/or N-doped ZnO nanoparticles, photocatalytic dye degradation was performed on **ZnO<sub>MOF-5</sub>**, **ZnO<sub>MOF-74</sub>** and **ZnO<sub>ZIF-8</sub>** under the same conditions mentioned above. As shown in Fig. S7a of Supplementary Data, **ZnO<sub>MOF-5</sub>** exhibited 34 % photodegradation compared to **ZnO<sub>Air</sub>** which showed 26 % photodegradation of MB after 6 hours irradiation under visible light. This improved activity can be attributed to the carbon doping in ZnO crystal lattice which results in narrowed energy band gap and better charge separation. However, samples **ZnO<sub>MOF-74</sub>** and **ZnO<sub>ZIF-8</sub>** demonstrated 14

% and 26 % photocatalytic activity respectively. It can be inferred that  $\text{ZnO}_{\text{MOF-5}}$  nanoparticles are more efficient photocatalysts compared to  $\text{ZnO}_{\text{MOF-74}}$  and  $\text{ZnO}_{\text{ZIF-8}}$ . This observation is consistent with the dye degradation results of ZnO/C composites shown in Fig. 12a. In addition, as presented in Fig. S8, the PXRD of  $\text{ZnO}/\text{C}_{\text{MOF-5}}$ ,  $\text{ZnO}/\text{C}_{\text{MOF-74}}$  and  $\text{ZnO}/\text{C}_{\text{ZIF-8}}$  composites after being used for dye photocatalytic degradation tests are identical to their fresh samples, which clearly confirm the crystalline and structural stability of these materials.

**Table 1** A comparison of photodegradation of MB by undoped and doped ZnO nanoparticles synthesized by different methods.

Catalyst	Dopant	Light source	Experimental conditions for photodegradation	Efficiency (%)		Ref.
				undoped	doped	
$\text{ZnO}/\text{C}_{\text{MOF-5}}$	C	120 mW/cm <sup>2</sup> 320 nm ≤ λ ≤ 780 nm	Catalyst = 200 mg/L MB = 20 mg/L	32	99.4	This work
$\text{ZnO}/\text{C}_{\text{MOF-74}}$	C	120 mW/cm <sup>2</sup> 320 nm ≤ λ ≤ 780 nm	Catalyst = 200 mg/L MB = 20 mg/L	14	92.2	This work
$\text{ZnO}/\text{C}_{\text{ZIF-8}}$	N	120 mW/cm <sup>2</sup> 320 nm ≤ λ ≤ 780 nm	Catalyst = 200 mg/L MB = 20 mg/L	26	94	This work
ZnO-C nanofibers	N	Solar simulator (Intensity = 80 lux) Philips18 W/54 1M7	Catalyst = 400 mg/L MB = 3.2 mg/L	13.9	42.3	[53]
ZnO	C	Intensity = 14.5 W/m <sup>2</sup>	-	8	41	[54]
ZnO@GO	-	40 W λ = 365 nm	Catalyst = 10 mg/L MB = 3.2 mg/L	49	98.5	[55]
C <sub>3</sub> N <sub>4</sub> /ZnO	-	1.2 mW/cm <sup>2</sup> λ > 400 nm	Catalyst = 500 mg/L MB = 10 mg/L	10	72.3	[56]
ZnO/PMMA	C, N	2 mW/cm <sup>2</sup> λ = 368 nm	Catalyst = 100 mg/L MB = 0.24 mg/L	7	60	[57]
C,N-ZnO	N	300 W Xe lamp	Catalyst = 250 mg/L MB = 10 mg/L	-	100	[36]
RGO/ZnO@ZIF-8		300 W Xe lamp λ > 420 nm	Catalyst = 1 g/L MB = 10 mg/L	46	82	[58]
Cu-ZnO	Cu	Sunlight	Catalyst = 1 g/L MB = 0.3 mg/L	92	90	[59]
Li-ZnO	Li	1000 W Xe lamp	Catalyst = 1.2 g/L MB = 3.2 mg/L	53.1	100	[60]
Hf-ZnO	Hf	Sunlight (1.263-105 lux)	Catalyst = 250 mg/L MB = 250 mg/L	50	85	[61]

As discussed above, the photocatalytic dye degradation and H<sub>2</sub> evolution under visible light critically depend on the energy band gap of semiconducting metal oxide nanoparticles.[62, 63] The generation of high numbers of electron-hole ( $e^-_{CB}/h^+_{VB}$ ) pairs upon absorption of incident visible light, the migration of these electrons and holes to the interfaces of the semiconductor nanoparticles and surface chemical reactions between the generated  $e^-/h^+$  and the targeted compounds (MB dye for degradation and H<sub>2</sub>O/MeOH for H<sub>2</sub> production) are three mechanistic steps of photocatalysis.[64] To improve the photocatalytic performance, narrow energy band gaps, less charge recombination of  $e^-$  and  $h^+$  and longer lifetime of excited charges are required. Due to the non-metal anionic C and/or N doping, hybridization of O<sub>2p</sub> and C<sub>2p</sub> and/or N<sub>2p</sub> orbitals takes place, creating a new energy level slightly above the valence band of ZnO nanoparticles. This additional energy level narrows the energy band gap between the valance and the conduction bands of ZnO nanoparticles and makes them photoactive semiconducting materials under visible light.[45, 65]

H<sub>2</sub> evolution results of **ZnO/C<sub>MOF-5</sub>**, **ZnO/C<sub>MOF-74</sub>** and **ZnO/C<sub>ZIF-8</sub>** are shown in Fig. 12b. Interestingly, **ZnO/C<sub>MOF-5</sub>** exhibited the highest H<sub>2</sub> evolution capacity of 25  $\mu\text{mol/g}$  after 6 hours while **ZnO/C<sub>MOF-74</sub>** and **ZnO/C<sub>ZIF-8</sub>** showed only 3 and 6  $\mu\text{mol/g}$  of H<sub>2</sub> evolution respectively under the same condition. As a reference, H<sub>2</sub> evolution by pure ZnO nanoparticles derived from the calcination of MOF-5 at 800 °C in the air (**ZnO<sub>Air</sub>**) was also measured under the same conditions. It showed that H<sub>2</sub> evolution capacity is only 0.8  $\mu\text{mol/g}$  (inset in Fig. S7b) which is negligible compared to **ZnO/C<sub>MOF-5</sub>**. To differentiate the role of doped carbon/nitrogen and the porous carbon matrix in H<sub>2</sub> generation, photocatalytic HER was also performed on ZnO nanoparticles obtained from re-calcination of MOF-derived ZnO/C composites under the same experimental conditions. As shown in Fig. S7b of Supplementary Data, **ZnO<sub>MOF-5</sub>**, **ZnO<sub>MOF-74</sub>** and **ZnO<sub>ZIF-8</sub>** demonstrated only 0.9, 0.2 and 0.6  $\mu\text{mol/g}$  H<sub>2</sub> evolution activity under the same experimental conditions respectively. Compared to that, ZnO nanoparticles embedded in the porous carbon matrix, **ZnO/C<sub>MOF-5</sub>**, **ZnO/C<sub>MOF-74</sub>** and **ZnO/C<sub>ZIF-8</sub>** showed 28, 15 and 10 times higher H<sub>2</sub> generation respectively. It is therefore confirmed that the porous carbon matrix plays a crucial role in charge ( $e^-/h^+$ ) transferring and preventing the charge recombination.

The improvement in H<sub>2</sub> evolution performance of ZnO/C composites can be understood through the schematic diagram shown in Fig. 11. The relatively higher H<sub>2</sub> evolution performance

(among ZnO/C composites) of **ZnO/C<sub>MOF-5</sub>** compared to **ZnO/C<sub>MOF-74</sub>** and **ZnO/C<sub>ZIF-8</sub>** might be due to the narrower energy band gap (UV-Vis absorption spectra), the higher amount of accessible mesopores and availability of more active sites (FTIR spectra). It can be assumed that due to higher amount of ZnO (83 wt.%, TGA) with better crystallinity of nanoparticles (confirmed by XPS and XRD) in catalyst **ZnO/C<sub>MOF-5</sub>**, more electrons are generated on surface upon interacting with visible light resulting in a higher reduction rate of H<sup>+</sup> and lesser charge (e<sup>-</sup>/h<sup>+</sup>) recombination. Consequently, more H<sub>2</sub> is generated. However, in **ZnO/C<sub>ZIF-8</sub>**, high content of carbon (TGA profiles) makes it difficult for visible light to penetrate deeper into the porous catalyst to access ZnO nanoparticles that are poorly crystalline. Furthermore, the generated electrons have longer diffusion length which causes loss of e<sup>-</sup>/h<sup>+</sup> pairs due to charge recombination. Therefore, this catalyst shows a relatively poor performance in H<sub>2</sub> evolution.

#### 4. Conclusions

Three different ZnO/C composites, derived from different MOFs at high temperature in water vapor saturated argon atmosphere, were systematic investigated and correlated with their precursors. The as-synthesized nanocomposites were further evaluated as photocatalysts for dye degradation and H<sub>2</sub> evolution under visible light. It was found that thermal decomposition of MOF-5 and MOF-74 under water-steam generate highly crystalline ZnO nanoparticles with high ZnO content whereas steam processing of ZIF-8 produces poor crystalline ZnO nanoparticles with the lower weight percentage of ZnO in the composites. The **ZnO/C<sub>MOF-5</sub>** show the highest thermal stability, **ZnO/C<sub>MOF-74</sub>** with moderate stability while **ZnO/C<sub>ZIF-8</sub>** are found to be thermally less resistant at high temperature. XPS and Raman analysis of derived composites confirm that C is the only dopant in **ZnO/C<sub>MOF-5</sub>** and **ZnO/C<sub>MOF-74</sub>**, while N plays the role of primary dopant in **ZnO/C<sub>ZIF-8</sub>**. Moreover, the thermal decomposition of methylimidazole linker in ZIF-8 gives more disordered carbon in resulting composite **ZnO/C<sub>ZIF-8</sub>** (more C-C sp<sup>3</sup> bonds). FTIR spectra demonstrate that there are more carboxyl (-COOH) functional groups presented on the surface of **ZnO/C<sub>MOF-5</sub>** due to the availability of more active sites on organic linker (terephthalic acid) as compared to **ZnO/C<sub>MOF-74</sub>** where the organic linker is 2,5-dihydroxyterephthalic acid. The high level of N present on the carbon surface in **ZnO/C<sub>ZIF-8</sub>** results in less oxygen-containing functionalities to attach on the surface of the catalyst under

these experimental conditions. SEM, TEM and EDX elemental mapping demonstrate that all three composites retain the morphologies of precursors and display well-dispersed ZnO nanoparticles homogeneously distributed in the porous carbon matrix. Due to the N and/or C doping, all three derived composites show red-shift in diffuse reflectance spectra, indicating the narrow energy band gaps (around 3.1 eV) as compared to the bulk ZnO (3.3 eV). The preservation of inherited textual properties in all three derived composites is confirmed by the calculated specific surface areas and pore size distributions. The appropriate pore sizes of nanocomposites facilitate the adsorption of organic dye onto the surface of the catalyst. Among these selected Zn-MOFs, the MOF-5 derived ZnO/C composite proved to be the best photocatalyst with the highest performance for MB dye degradation and H<sub>2</sub> evolution under visible light.

### Acknowledgements

The financial support by EPSRC CDT in Metamaterials at University of Exeter and EU RFCS (RFCS-2016-754077) is greatly acknowledged.

### Appendix A. Supplementary data

Supplementary data related to this article can be found in the file attached.

### References

- [1] H. Wu, Q. Gong, D.H. Olson, J. Li, Commensurate adsorption of hydrocarbons and alcohols in microporous metal organic frameworks, *Chem. Rev.* 112 (2012) 836-868.
- [2] R. Banerjee, H. Furukawa, D. Britt, C. Knobler, M. O’Keeffe, O.M. Yaghi, Control of pore size and functionality in isorecticular zeolitic imidazolate frameworks and their carbon dioxide selective capture properties, *J. Am. Chem. Soc.* 131 (2009) 3875-3877.
- [3] D. Sheberla, J.C. Bachman, J.S. Elias, C.-J. Sun, Y. Shao-Horn, M. Dincă, Conductive MOF electrodes for stable supercapacitors with high areal capacitance, *Nature Mater.* 16 (2016) 220.

- [4] M. Yoon, R. Srirambalaji, K. Kim, Homochiral metal–organic frameworks for asymmetric heterogeneous catalysis, *Chem. Rev.* 112 (2012) 1196-1231.
- [5] A. Dhakshinamoorthy, Z. Li, H. Garcia, Catalysis and photocatalysis by metal organic frameworks, *Chem. Soc. Rev.* (2018).
- [6] E.A. Dolgoplova, A.M. Rice, C.R. Martin, N.B. Shustova, Photochemistry and photophysics of MOFs: steps towards MOF-based sensing enhancements, *Chem. Soc. Rev.* 47 (2018) 4710-4728.
- [7] Y. Chen, D. Wang, X. Deng, Z. Li, Metal–organic frameworks (MOFs) for photocatalytic CO<sub>2</sub> reduction, *Catal. Sci. Technol.* 7 (2017) 4893-4904.
- [8] H. Li, M. Eddaoudi, M. O'Keeffe, O.M. Yaghi, Design and synthesis of an exceptionally stable and highly porous metal-organic framework, *Nature* 402 (1999) 276.
- [9] M.A. Nasalevich, M. van der Veen, F. Kapteijn, J. Gascon, Metal–organic frameworks as heterogeneous photocatalysts: advantages and challenges, *CrystEngComm* 16 (2014) 4919-4926.
- [10] C.-C. Wang, J.-R. Li, X.-L. Lv, Y.-Q. Zhang, G. Guo, Photocatalytic organic pollutants degradation in metal–organic frameworks, *Energy Environ. Sci.* 7 (2014) 2831-2867.
- [11] H.-P. Jing, C.-C. Wang, Y.-W. Zhang, P. Wang, R. Li, Photocatalytic degradation of methylene blue in ZIF-8, *RSC Adv.* 4 (2014) 54454-54462.
- [12] T. Toyao, M. Saito, Y. Horiuchi, K. Mochizuki, M. Iwata, H. Higashimura, et al., Efficient hydrogen production and photocatalytic reduction of nitrobenzene over a visible-light-responsive metal–organic framework photocatalyst, *Catal. Sci. Technol.* 3 (2013) 2092-2097.
- [13] Q. Yu, H. Dong, X. Zhang, Y.-X. Zhu, J.-H. Wang, F.-M. Zhang, et al., Novel stable metal–organic framework photocatalyst for light-driven hydrogen production, *CrystEngComm* 20 (2018) 3228-3233.
- [14] C.B. Ong, L.Y. Ng, A.W. Mohammad, A review of ZnO nanoparticles as solar photocatalysts: Synthesis, mechanisms and applications, *Renew. Sustain. Energy Rev.* 81 (2018) 536-551.
- [15] K.M. Lee, C.W. Lai, K.S. Ngai, J.C. Juan, Recent developments of zinc oxide based photocatalyst in water treatment technology: A review, *Water Res.* 88 (2016) 428-448.

- [16] L. Oar-Arteta, T. Wezendonk, X. Sun, F. Kapteijn, J. Gascon, Metal organic frameworks as precursors for the manufacture of advanced catalytic materials, *Mater. Chem. Front.* 1 (2017) 1709-1745.
- [17] Z. Xie, W. Xu, X. Cui, Y. Wang, Recent progress in metal–organic frameworks and their derived nanostructures for energy and environmental applications, *ChemSusChem* 10 (2017) 1645-1663.
- [18] Y.Z. Chen, R. Zhang, L. Jiao, H.-L. Jiang, Metal–organic framework-derived porous materials for catalysis, 2018.
- [19] Y.V. Kaneti, J. Tang, R.R. Salunkhe, X. Jiang, A. Yu, K.C.-W. Wu, et al., Nanoarchitected design of porous materials and nanocomposites from metal-organic frameworks, *Adv. Mater.* 29 (2017) 1604898.
- [20] R. Das, P. Pachfule, R. Banerjee, P. Poddar, Metal and metal oxide nanoparticle synthesis from metal organic frameworks (MOFs): finding the border of metal and metal oxides, *Nanoscale* 4 (2012) 591-599.
- [21] P.A. Julien, K. Užarević, A.D. Katsenis, S.A.J. Kimber, T. Wang, O.K. Farha, et al., In situ monitoring and mechanism of the mechanochemical formation of a microporous MOF-74 framework, *J. Am. Chem. Soc.* 138 (2016) 2929-2932.
- [22] P. Liang, C. Zhang, H. Sun, S. Liu, M. Tade, S. Wang, Solar photocatalytic water Oxidation and purification on ZIF-8-derived C–N–ZnO composites, *Energy Fuels* 31 (2017) 2138-2143.
- [23] S. Gadipelli, Z. Guo, Postsynthesis annealing of MOF-5 remarkably enhances the framework structural stability and CO<sub>2</sub> uptake, *Chem. Mater.* 26 (2014) 6333-6338.
- [24] B. Chen, G. Ma, D. Kong, Y. Zhu, Y. Xia, Atomically homogeneous dispersed ZnO/N-doped nanoporous carbon composites with enhanced CO<sub>2</sub> uptake capacities and high efficient organic pollutants removal from water, *Carbon* 95 (2015) 113-124.
- [25] Y. Song, X. Li, L. Sun, L. Wang, Metal/metal oxide nanostructures derived from metal–organic frameworks, *RSC Adv.* 5 (2015) 7267-7279.
- [26] R.R. Salunkhe, Y.V. Kaneti, Y. Yamauchi, Metal–organic framework-derived nanoporous metal oxides toward supercapacitor applications: Progress and prospects, *ACS Nano* 11 (2017) 5293-5308.

- [27] D.J. Tranchemontagne, J.R. Hunt, O.M. Yaghi, Room temperature synthesis of metal-organic frameworks: MOF-5, MOF-74, MOF-177, MOF-199, and IRMOF-0, *Tetrahedron* 64 (2008) 8553-8557.
- [28] J. Cravillon, S. Münzer, S.-J. Lohmeier, A. Feldhoff, K. Huber, M. Wiebcke, Rapid room-temperature synthesis and characterization of nanocrystals of a prototypical zeolitic imidazolate framework, *Chem. Mater.* 21 (2009) 1410-1412.
- [29] L. Zhang, Y.H. Hu, A systematic investigation of decomposition of Nano  $Zn_4O(C_8H_4O_4)_3$  metal-organic framework, *J. Phys. Chem. C* 114 (2010) 2566-2572.
- [30] N.L. Rosi, J. Kim, M. Eddaoudi, B. Chen, M. O'Keeffe, O.M. Yaghi, Rod packings and metal-organic frameworks constructed from rod-shaped secondary building units, *J. Am. Chem. Soc.* 127 (2005) 1504-1518.
- [31] J.B. James, Y.S. Lin, Kinetics of ZIF-8 thermal decomposition in inert, oxidizing, and reducing environments, *J. Phys. Chem. C* 120 (2016) 14015-14026.
- [32] B. Xu, Y. Mei, Z. Xiao, Z. Kang, R. Wang, D. Sun, Monitoring thermally induced structural deformation and framework decomposition of ZIF-8 through in situ temperature dependent measurements, *Phys. Chem. Chem. Phys.* 19 (2017) 27178-27183.
- [33] S. Gadipelli, Z.X. Guo, Tuning of ZIF-derived carbon with high activity, nitrogen functionality, and yield – A case for superior  $CO_2$  capture, *ChemSusChem* 8 (2015) 2123-2132.
- [34] A.S. Alshammari, L. Chi, X. Chen, A. Bagabas, D. Kramer, A. Alromaeh, et al., Visible-light photocatalysis on C-doped ZnO derived from polymer-assisted pyrolysis, *RSC Adv.* 5 (2015) 27690-27698.
- [35] P. Liang, C. Zhang, H. Sun, S. Liu, M. Tadé, S. Wang, Photocatalysis of C, N-doped ZnO derived from ZIF-8 for dye degradation and water oxidation, *RSC Adv.* 6 (2016) 95903-95909.
- [36] U. Ozgur, Y. I. Alivov, C. Liu, A. Teke, M. A. Reshchikov, S. Dogan, et al., A comprehensive review of ZnO materials and devices, *J. Appl. Phys.* 98 (2005) 041301.
- [37] M. Wang, F. Ren, J. Zhou, G. Cai, L. Cai, Y. Hu, et al., N Doping to ZnO nanorods for photoelectrochemical water splitting under visible light: Engineered impurity distribution and terraced band structure, *Sci. Rep.*, 5 (2015) 12925.

- [38] H. Sudrajat, S. Babel, Comparison and mechanism of photocatalytic activities of N-ZnO and N-ZrO<sub>2</sub> for the degradation of rhodamine 6G, *Environ. Sci. Pollut. Res.* 23 (2016) 10177-10188.
- [39] A.C. Ferrari, J. Robertson, Interpretation of Raman spectra of disordered and amorphous carbon, *Phys. Rev. B* 61 (2000) 14095-14107.
- [40] F.J. Manjón, B. Marí, J. Serrano, A.H. Romero, Silent Raman modes in zinc oxide and related nitrides, *J. Appl. Phys.* 97 (2005) 053516.
- [41] A. Kaschner, U. Haboek, M. Strassburg, M. Strassburg, G. Kaczmarczyk, A. Hoffmann, et al., Nitrogen-related local vibrational modes in ZnO:N, *Appl. Phys. Lett.* 80 (2002) 1909-1911.
- [42] S. Sun, X. Chang, X. Li, Z. Li, Synthesis of N-doped ZnO nanoparticles with improved photocatalytic activity, *Ceram. Int.* 39 (2013) 5197-5203.
- [43] D.K. Mishra, J. Mohapatra, M.K. Sharma, R. Chattarjee, S.K. Singh, S. Varma, et al., Carbon doped ZnO: Synthesis, characterization and interpretation, *J. Magnet. Magnet. Mater.* 329 (2013) 146-152.
- [44] A.C. Ferrari, J. Robertson, Interpretation of Raman spectra of disordered and amorphous carbon, *Phys. Rev. B* 61 (2000) 14095-14107.
- [45] H.-X. Zhong, J. Wang, Y.-W. Zhang, W.-L. Xu, W. Xing, D. Xu, et al., ZIF-8 Derived graphene-based nitrogen-doped porous carbon sheets as highly efficient and durable oxygen reduction electrocatalysts, *Angew. Chem. Int. Ed.* 53 (2014) 14235-14239.
- [46] S.S. Kaye, A. Dailly, O.M. Yaghi, J.R. Long, Impact of preparation and handling on the hydrogen storage properties of Zn<sub>4</sub>O(1,4-benzenedicarboxylate)<sub>3</sub> (MOF-5), *J. Am. Chem. Soc.* 129 (2007) 14176-14177.
- [47] J.M. Simmons, H. Wu, W. Zhou, T. Yildirim, Carbon capture in metal-organic frameworks—a comparative study, *Energy Environ. Sci.* 4 (2011) 2177-2185.
- [48] H. Wu, W. Zhou, T. Yildirim, High-capacity methane storage in metal-organic frameworks M<sub>2</sub>(dhtp): The important role of open metal sites, *J. Am. Chem. Soc.* 131 (2009) 4995-5000.
- [49] G. Srinivas, V. Krungleviciute, Z.-X. Guo, T. Yildirim, Exceptional CO<sub>2</sub> capture in a hierarchically porous carbon with simultaneous high surface area and pore volume, *Energy Environ. Sci.* 7 (2014) 335-342.

- [50] Y. Zhang, J. Zhou, X. Chen, Q. Feng, W. Cai, MOF-derived C-doped ZnO composites for enhanced photocatalytic performance under visible light, *J. Alloys. Comp.* 777 (2019) 109-118.
- [51] T. Hisatomi, J. Kubota, K. Domen, Recent advances in semiconductors for photocatalytic and photoelectrochemical water splitting, *Chem. Soc. Rev.* 43 (2014) 7520-7535.
- [52] E. Antolini, Photo-assisted methanol oxidation on Pt-TiO<sub>2</sub> catalysts for direct methanol fuel cells: A short review, *Appl. Catal. B Environ.* 237 (2018) 491-503.
- [53] M. Samadi, H.A. Shivaee, A. Pourjavadi, A.Z. Moshfegh, Synergism of oxygen vacancy and carbonaceous species on enhanced photocatalytic activity of electrospun ZnO-carbon nanofibers: Charge carrier scavengers mechanism, *Appl. Catal. A Gen.* 466 (2013) 153-160.
- [54] B.M. Rajbongshi, A. Ramchiary, S.K. Samdarshi, Influence of N-doping on photocatalytic activity of ZnO nanoparticles under visible light irradiation, *Mater. Lett.*, 134 (2014) 111-114.
- [55] R. Atchudan, T.N.J.I. Edison, S. Perumal, D. Karthikeyan, Y.R. Lee, Facile synthesis of zinc oxide nanoparticles decorated graphene oxide composite via simple solvothermal route and their photocatalytic activity on methylene blue degradation, *J. Photochem. Photobio. B* 162 (2016) 500-510.
- [56] Y. Wang, R. Shi, J. Lin, Y. Zhu, Enhancement of photocurrent and photocatalytic activity of ZnO hybridized with graphite-like C<sub>3</sub>N<sub>4</sub>, *Energy Environ. Sci.* 4 (2011) 2922-2929.
- [57] A. Di Mauro, M. Cantarella, G. Nicotra, G. Pellegrino, A. Gulino, M.V. Brundo, et al., Novel synthesis of ZnO/PMMA nanocomposites for photocatalytic applications, *Sci. Rep.* 7 (2017) 40895.
- [58] G. Zhu, X. Li, H. Wang, L. Zhang, Microwave assisted synthesis of reduced graphene oxide incorporated MOF-derived ZnO composites for photocatalytic application, *Catal. Commun.* 88 (2017) 5-8.
- [59] S. Kuriakose, B. Satpati, S. Mohapatra, Highly efficient photocatalytic degradation of organic dyes by Cu doped ZnO nanostructures, *Phys. Chem. Chem. Phys.* 17 (2015) 25172-25181.

- [60] I. Ganesh, P.S.C. Sekhar, G. Padmanabham, G. Sundararajan, Influence of Li-doping on structural characteristics and photocatalytic activity of ZnO nano-powder formed in a novel solution pyro-hydrolysis route, *Appl. Surf. Sci.* 259 (2012) 524-537.
- [61] M. Ahmad, E. Ahmed, Z.L. Hong, Z. Iqbal, N.R. Khalid, T. Abbas, et al., Structural, optical and photocatalytic properties of hafnium doped zinc oxide nanophotocatalyst, *Ceram. Int.* 39 (2013) 8693-8700.
- [62] H. Ahmad, S.K. Kamarudin, L.J. Minggu, M. Kassim, Hydrogen from photo-catalytic water splitting process: A review, *Renew. Sustain. Energy Rev.* 43 (2015) 599-610.
- [63] F. Song, W. Li, Y. Sun, Metal–organic frameworks and their derivatives for photocatalytic water splitting, *Inorganics* 5 (2017) 40.
- [64] K. Maeda, Z-Scheme water splitting using two different semiconductor photocatalysts, *ACS Catal.* 3 (2013) 1486-1503.
- [65] L. Pan, T. Muhammad, L. Ma, Z.-F. Huang, S. Wang, L. Wang, et al., MOF-derived C-doped ZnO prepared via a two-step calcination for efficient photocatalysis, *Appl. Catal. B Environ.* 189 (2016) 181-191.